Journal of Nanobiotechnology

RESEARCH

Open Access

Targeting ferroptosis to rescue osteogenic differentiation in BRONJ-affected jawbone mesenchymal stem cells: the role of miR-145-3p and exosome-mediated therapy

Yi Shuai[1,2*†], Bo Chen[1,2†], Tao Jiang[1,2†], Lei Zhu[1,2], Han Su[1,2], Wei Wei[1,2], Bingyao Liu[3*] and Lei Jin[4*]

Abstract

Background Bisphosphonate-related osteonecrosis of the jaw (BRONJ) is a severe, therapy-refractory condition driven by ferroptotic disruption of jawbone-derived mesenchymal stem cells (MSCs) biology. We dissect this mechanism to validate ferroptosis as a therapeutic target.

Methods We first demonstrated that miR-145-3p is mechanistically coupled to ferroptosis and osteogenesis in BRONJ model by gain- and loss-of-function studies. To evaluate therapeutic efficacy under pathologically relevant conditions, we designed three models: (i) Local BRONJ repair model: miR-145-3p-enriched exosomes were encapsulated in an injectable hydrogel scaffold and grafted into necrotic alveolar bone to assess direct BRONJ resolution. After local BRONJ treatment, endogenous MSCs were re-isolated, and both cellular and exosomal miR-145-3p levels were quantified. (ii) Osteoporosis treatment model: The reprogrammed MSCs derived from treated BRONJ rats were then administered intravenously to osteoporotic littermates to evaluate whether these MSCs retain systemic osteogenic competence. (iii) Critical-sized calvarial defect repair model: To further dissect the intrinsic osteogenic capacity, reprogrammed MSCs derived from treated BRONJ rats were fabricated into cell-sheet/HA-TCP "sandwich" constructs and transplanted into calvarial defects.

Results BRONJ markedly compromised MSCs viability while elevating hallmarks of ferroptosis that were reversed by the ferroptosis inhibitor. Concomitantly, osteogenic capacity declined, as shown by reduced ALP activity, mineralized nodules, new bone formation and expression of RUNX2 and OCN. Mechanistically, we identified a miR-145-3p/IREB2 regulatory circuit that governs ferroptosis in BRONJ-derived MSCs; exosome-mediated delivery of miR-145-3p reinstated this axis, thereby reactivating the MSCs osteogenesis and driving in situ bone regeneration. Critically,

†Yi Shuai, Bo Chen and Tao Jiang contributed equally to this work.

*Correspondence:
Yi Shuai
handsy@126.com
Bingyao Liu
544791829@qq.com
Lei Jin
ljin666666@zju.edu.cn

Full list of author information is available at the end of the article

after local BRONJ therapy, the reprogrammed MSCs were (i) infused via tail vein into osteoporotic rats, significantly elevating bone mass, and (ii) engineered into cell-sheet/HA-TCP "sandwich" constructs that achieved robust repair of critical-sized calvarial defects. These data establish exosomal miR-145-3p as a therapeutic that mitigates ferroptosis and restores the osteogenic competence of jawbone-derived MSCs for bone regeneration.

Conclusion Collectively, our findings establish the miR-145-3p/IREB2/ferroptosis axis as an important regulator of BRONJ pathology and demonstrate that exosomal delivery of miR-145-3p not only ameliorates localized BRONJ but also substantially reinstates the systemic osteogenic potential of jawbone-derived MSCs, offering a pre-clinical promising strategy to combat both BRONJ and associated bone loss disorders.

Keywords BRONJ, Ferroptosis, Mesenchymal stem cells, Osteogenic differentiation, MiR-145-3p, Exosomes

Graphical Abstract

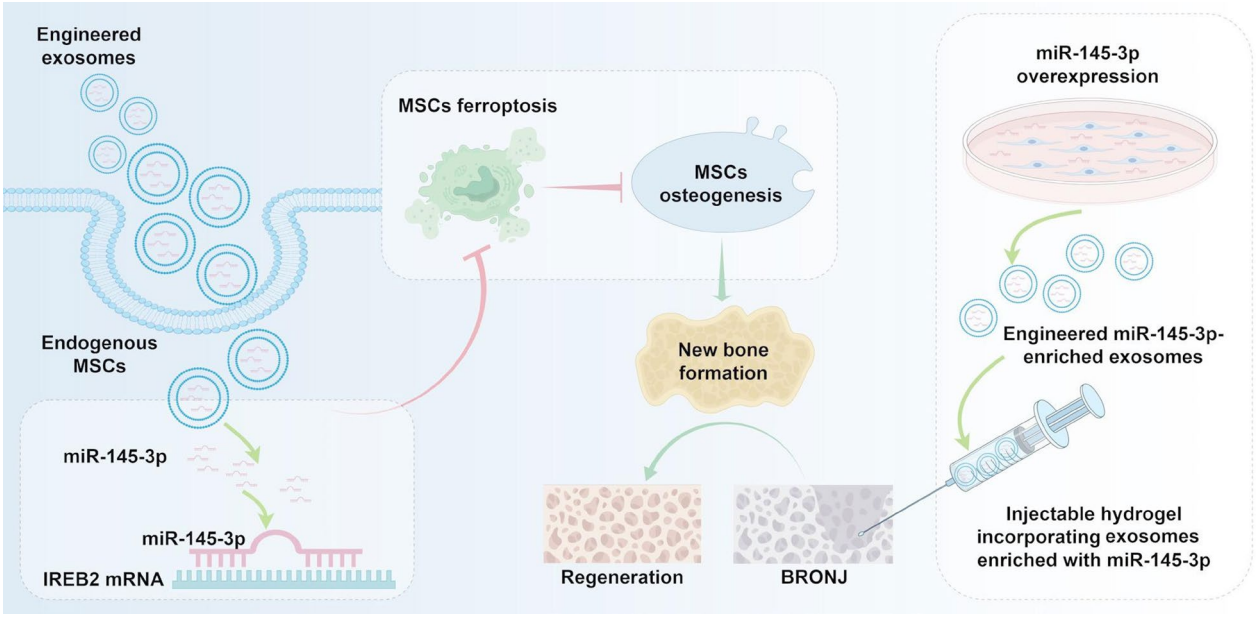

Introduction

BRONJ is an orphan disease with significant morbidity, arising as a severe complication from the use of bisphosphonates, which are widely prescribed for osteoporosis and malignancy-related bone diseases [1, 2]. This condition is characterized by the exposure of necrotic bone in the maxillofacial region that fails to heal over time, leading to not only potential functional impairment, but also poor quality of life causing pain, infection and aesthetic concerns [1, 2]. Current therapeutic strategies for BRONJ, including surgical debridement and drug administration, are often limited by their invasiveness, high risk of complications, and suboptimal outcomes [1, 2]. Therefore, there is an urgent need to explore novel therapeutic approaches that can effectively promote bone regeneration and alleviate the symptoms of BRONJ. The pathogenesis of BRONJ remains elusive; however, it is hypothesized that the disease involves a complex interplay of bisphosphonate-induced suppression of osteoclast and osteoblast activity, angiogenesis disruption, and cellular stress responses [3].

Recent research has begun to unravel the role of ferroptosis, a non-apoptotic form of cell death associated with the accumulation of lipid peroxidation products and iron metabolism dysregulation, in the context of cancer [4], neurodegenerative diseases [5], and ischemia-reperfusion injury [6], and is increasingly recognized for its potential role in bone diseases [7, 8]. Studies have highlighted the interplay between iron homeostasis and bone metabolism, with iron overload or deficiency being implicated in the pathogenesis of osteoporosis [7, 9]. Iron metabolism disorders can promote osteoclast differentiation [10] and apoptosis of osteoblasts [11], while also inhibiting the proliferation and differentiation of osteoblasts [12], ultimately disrupting the balance of bone remodeling. In addition, ferroptosis also impedes the osteogenesis of the MSCs [13]. The relationship between iron metabolism and osteoporosis offers new insights for clinical treatment and drug development, underscoring the importance of understanding and targeting iron metabolism in bone health and disease.

MicroRNAs (miRNAs) are pivotal regulators in bone metabolism, influencing the proliferation and differentiation of bone cells such as MSCs, osteoblasts and osteoclasts [14]. They modulate bone formation and resorption by targeting various osteogenic and osteoclastic factors, thereby impacting the balance of bone homeostasis [14]. In the context of ferroptosis, miRNAs have emerged as significant players. They can precisely modulate the expression of genes involved in iron metabolism, lipid peroxidation and antioxidant defenses, which are crucial in the pathogenesis of diseases where ferroptosis is implicated [15–17]. The interplay between miRNAs and ferroptosis has implications for disease pathogenesis and potential therapeutic interventions, offering a new approach for understanding and treating conditions associated with bone metabolism and iron-dependent cell death. MiR-145 has been demonstrated to regulate ferroptosis and maintain cellular health across a range of cell types [18, 19]. Our earlier research indicated a reduction in circulating miR-145 levels in BRONJ-affected rats [20], highlighting its potential as a key player in the pathogenesis of BRONJ. Building on these findings, we aim to investigate the impact of miR-145-3p on ferroptosis and osteogenic differentiation in MSCs compromised by BRONJ.

Exosomes, as nanoscale vesicles released by cells, have emerged as a promising therapeutic tool in regenerative medicine [21, 22]. They possess several unique advantages, including low immunogenicity, good biocompatibility, and the ability to deliver bioactive molecules such as miRNAs to target cells. In the field of bone tissue engineering, exosomes have been shown to promote osteogenesis, angiogenesis and tissue repair [22–24]. For example, studies have demonstrated that exosomes can enhance bone regeneration in animal models of osteoporosis [7, 25] and fracture healing [24, 26]. These findings suggest that exosome-based therapies hold great potential for the treatment of BRONJ by modulating the biological functions of endogenous cells and promoting bone repair.

In this research, our objective was to uncover the regulatory function of miR-145-3p in BRONJ and to develop an innovative therapeutic approach leveraging engineered exosomes. Our strategy was designed to suppress ferroptosis and enhance the repair of osteonecrosis, thereby unveiling a new mechanistic understanding and offering a promising therapeutic approach for the management of BRONJ.

Methods

Ethics

All animal experimental protocols were reviewed and approved by the Department of Comparative Medicine at Jinling Hospital, Affiliated Hospital of Medical School, Nanjing University (Permit No. 2021DZGKJD-WLS-0090), strictly adhering to the guidelines set forth by the NIH for the Care and Use of Laboratory Animals.

Animals

All experimental animals were sourced from the Animal Center of the Department of Comparative Medicine at Jinling Hospital, Affiliated Hospital of Medical School, Nanjing University. We utilized eight-week-old female Sprague Dawley (SD) rats for the establishment of models, including BRONJ, ovariectomy (OVX)-induced osteoporosis, and critical-sized calvarial defect models. These rats also served as the subjects for MSCs collection, which was conducted for exosome preparation and subsequent in vitro analyses. For the ectopic bone formation assay, we employed eight-week-old female NOD/SCID mice. The animals were maintained under specific pathogen-free conditions, with an ambient temperature of 22 °C, a 12-hour light/dark cycle, and a relative humidity of 50%–55%. They were provided with continuous access to standard food pellets and tap water throughout the study.

Establishment of BRONJ model

For BRONJ model, female SD rats aged 8 weeks were administered zoledronic acid (80 μg/kg) and dexamethasone (1 mg/kg) (both from Sigma-Aldrich, USA) via tail vein injection once a week for 13 consecutive weeks, followed by the extraction of the maxillary first molar. For control model, female SD rats received a tail vein injection of an equal volume of phosphate-buffered saline (PBS) (Gibco, USA) while undergoing all other procedures exactly as described for the BRONJ model.

Isolation and culture of jawbone MSCs

For the cultivation of rat MSCs from the jawbone, the entire bone marrow was extracted by flushing the jawbone with α-MEM (Gibco) with 10% FBS (Gibco). The cell count was determined using an electronic cell counter (Bio-Rad, USA). On average, approximately 8.0×10^7 bone marrow cells were then seeded at a density of 8.0×10^7 per dish in 10-cm plastic petri dishes (ThermoFisher Scientific, USA). Prior to their use in subsequent experiments, MSCs were verified for their mesenchymal stem cell properties.

Flow cytometry

A single-cell suspension of 5×10^5 MSCs (passage 2) was prepared and incubated with a panel of antibodies specific to rat CD29 (Santa Cruz Biotechnology, USA), CD90 and CD45 (BD Bioscience, USA). This incubation was conducted at 4 °C in the absence of light to prevent photobleaching of the fluorophores. Subsequently, the samples were subjected to flow-cytometric analysis to

characterize the stem cell surface markers. This analysis was performed using a Beckman Coulter Epics XL cytometer, an instrument from Beckman Coulter, USA, which provided identification of the cellular markers.

Fibroblastic colony-forming assay

5×10^2 MSCs (passage 2) were plated in a 5-cm plastic petri dish (ThermoFisher Scientific) with α-MEM medium (Gibco). The medium was changed every 3 days to ensure nutrient replenishment and waste removal. After a 10-day cultivation period, the dishes were gently rinsed with PBS (Gibco) to remove any debris, and the cells were fixed using 4% paraformaldehyde (Beyotime, China). The colonies were then stained with 0.5% crystal violet (Beyotime): the dye was prepared by diluting the stock solution in PBS (Gibco) to a final concentration of 0.5% (w/v), applied for 15 min at room temperature, and then gently rinsed three times with PBS (Gibco) to remove excess stain. Under a stereomicroscope (Olympus Optical, Japan), cell aggregates consisting of more than 50 cells were identified as colonies. The colony-forming efficiency was determined by calculating the ratio of the number of colonies to 200 cells expressed as a percentage.

Alizarin red S staining

In the assessment of osteogenic differentiation, 1×10^5 MSCs (passage 2) per well were seeded into 12-well plates (ThermoFisher Scientific). Once the cells achieved 80% confluence, an osteogenic medium was introduced, comprising 5 mM β-glycerophosphate, 50 μg/mL ascorbic acid, and 10 nM dexamethasone (all from Sigma-Aldrich). This medium was replenished every 3 days to maintain optimal conditions for osteogenic differentiation. For Alizarin Red S staining, the cells were cultured in osteogenic medium for a duration of 28 days. The staining was performed according to the instructions provided (Beyotime). Quantification involved dissolving the stained mineralized nodules in 6% cetyl-pyridine (Beyotime), and the optical density (OD) was measured using a microplate reader (Bio-TEK Instruments, USA) at a wavelength of 570 nm.

Oil red O staining

In course of the adipogenic differentiation assay, MSCs (passage 2) were cultivated for a period of 14 days in a specialized adipogenic differentiation medium. This medium was enriched with 0.5 μM dexamethasone, 0.5 mM isobutylmethylxanthine, and 60 μM indomethacin, all procured from Sigma-Aldrich. To visualize the lipid accumulation within the cells, the lipid droplets were stained using an Oil Red O solution (Beyotime). The resulting lipid droplets were then examined under a stereomicroscope provided by Olympus Optical. Quantification involved dissolving the Oil red O in 100% isopropanol (Beyotime) at room temperature for 5 min, and the OD was measured using a microplate reader (Bio-TEK Instruments) at a wavelength of 510 nm.

In vitro specific Inhibition of ferroptosis

Based on a gradient concentration screen of 0 μM, 0.1 μM, 1 μM, 5 μM, 10 μM, 20 μM, and 50 μM, 10 μM of Ferrostatin-1 (Fer-1) (Sigma-Aldrich) was ultimately identified as the optimal treatment concentration. The MSCs (passage 2) were cultured to approximately 80% confluence in a 6-well plate (ThermoFisher Scientific), the specific ferroptosis inhibitor Fer-1 was added in vitro at a concentration of 10 μM. Prior to treatment, the culture medium was aspirated, and the cells were washed once with pre-warmed PBS (Gibco) to remove any residual medium. Then, 2 mL of fresh medium containing Fer-1 was added to each well, ensuring that the final concentration of Fer-1 was 10 μM. The plates were gently rocked to ensure even distribution of the inhibitor and then incubated at 37 °C with 5% CO_2 for 1 h to allow the cells to pre-incubate with Fer-1 before further experimental manipulation.

Cell survival assay

MSCs (passage 2) were seeded at a density of 1×10^3 cells per well in 96-well plates (ThermoFisher Scientific) and incubated for 8 h before testing. Cell survival was assessed using the cell counting kit-8 (CCK-8) (Beyotime) according to the manufacturer's standard protocol. To elaborate, 10 μL of the CCK-8 solution was added to each well containing 100 μL of medium, and the plates were subsequently incubated at 37 °C with saturated humidity and 5% CO_2 for 2 h after gentle mixing. The OD values were then measured using a microplate reader (BioTek Instruments) at a wavelength of 450 nm.

To calculate the cell survival, the following formula was applied: Cell survival (%)= $[(OD_{experimental}-OD_{blank})/(OD_{control}-OD_{blank})]\times 100\%$. This formula allowed for the determination of the relative cell survival rate by comparing the optical density readings of the experimental wells to those of the control and blank wells.

Iron assay

MSCs at passage 2 were used for iron assay. To conduct the iron assay, throughout the procedure, adhere to the instructions provided in the assay kit (Abcam, USA). Briefly, to specifically quantify Fe^{2+} only, the standard protocol was modified as follows: serial standards (100 μL) and samples (2–50 μL, adjusted to 100 μL with Iron Assay Buffer) were loaded in duplicate. All wells, including both standards and samples, received 5 μL of Assay Buffer; the Iron Reducer was omitted entirely. After gentle agitation, plates were incubated at 37 °C for 30 min,

followed by addition of 100 μL Iron Probe to all wells and a further 60 min incubation at 37 °C in darkness. Absorbance was read immediately at 593 nm on a microplate reader (BioTek Instruments).

Lipid peroxidation (MDA) assay

MSCs at passage 2 were used for MDA assay. To conduct the MDA assay, throughout the procedure, adhere to the instructions provided in the assay kit (Abcam). To generate MDA-TBA adducts, combine 200 μL of each standard or sample with 600 μL Developer VII/TBA reagent and heat at 95 °C for 60 min. After rapid cooling on ice (10 min), any residual turbidity is eliminated by passage through a 0.2 μm syringe filter. Although Developer VII/TBA can react with other sample constituents, these side reactions do not compromise MDA quantitation. Transfer 200 μL of the clarified reaction mixture to a 96-well plate (ThermoFisher Scientific); the standard curve spans 0–5 nmol MDA for colorimetry and 0–0.5.5 nmol MDA for fluorometry. Read absorbance at 532 nm immediately after plating.

Western blot analysis

MSCs (passage 2) were lysed using a cell lysis buffer enriched with protease inhibitors, as well as through ultrasonication at a low frequency. Following centrifugation, the resulting precipitates were discarded, and the supernatant, which contained the total protein content, was collected for subsequent western blot analysis. Equal quantities of proteins were loaded onto a 15% SDS-PAGE gel. After electrophoretic separation, the proteins were transferred onto polyvinylidene fluoride membranes (Millipore, USA). The membranes were initially blocked with a 5% BSA blocking buffer (Beyotime) and then incubated for 12 h at 4 °C with primary antibodies specific to rat glutathione peroxidase 4 (GPX4) (Cell Signaling Technology, USA), IREB2 (Abcam), and β-actin (Cell Signaling Technology). Subsequently, the membranes were incubated with a secondary antibody (Boster, China) at room temperature for 2 h, after which they were rinsed. The protein bands on the membranes were visualized using a protein enhancement imaging system with an enhanced chemiluminescence kit (Boster). The gray values of these bands were quantified using ImageJ software (v1.8.0, NIH, USA). Each band's value was normalized relative to the corresponding β-actin value.

Transmission electron microscopy (TEM) analysis of mitochondrial morphology

To prepare MSCs (passage 2) for TEM analysis, the cells are initially cultured to the desired density in a flask using α-MEM (Gibco) with 10% FBS (Gibco). Once they reach confluence, the medium is removed, and the cells are washed with PBS (Gibco) before being detached with Trypsin-EDTA (Gibco) and collected in a centrifuge tube (ThermoFisher Scientific). To preserve ultrastructure, cells were fixed for 2 h at 4 °C with 2.5% glutaraldehyde (Electron Microscopy Sciences, USA) in 0.1 M sodium cacodylate buffer (Electron Microscopy Sciences). To enhance contrast, the cells are then postfix-fixed with 1% osmium tetroxide (Electron Microscopy Sciences) in the same buffer for 1 h at 4 °C, followed by staining with 2% uranyl acetate (Electron Microscopy Sciences) in distilled water for 12 h at 4 °C. Subsequently, the cells are dehydrated through a graded ethanol series (30% to 100%) at 4 °C, infiltrated, and embedded in Spurr's resin (Electron Microscopy Sciences) within molds. After polymerizing the embedded cells at 60 °C for 48 h, the blocks are trimmed, and ultrathin sections (70 nm) are cut using an ultramicrotome and mounted on 200-mesh copper grids (Leica Microsystems, USA). These sections are then stained with lead citrate (Electron Microscopy Sciences) for 5 min to further enhance contrast. Finally, the sections are examined under a TEM (Carl Zeiss, Germany) at the appropriate magnification to visualize mitochondrial morphology and capture high-resolution images for analysis of mitochondrial size and membrane density.

Mitochondrial size was determined from TEM micrographs acquired at 20,000× on 70 nm ultrathin sections with clearly resolved organellar contours and cristae. After importing the images into ImageJ software (v1.8.0, NIH), spatial calibration was performed using the Set Scale command with a calibrated pixel size of 0.5 nm. The long axis was measured with the Straight-Line tool drawn along the longest chord; the short axis was measured perpendicular to this chord at its widest point. Organelle cross-sectional area was obtained by manually tracing the outer mitochondrial membrane with the Freehand Selection tool followed by Measure. For each experimental condition, 10 mitochondria from 4 biological replicates were analyzed.

To quantify the relative mitochondrial membrane density in TEM images, digital micrographs are first calibrated for pixel-to-nanometer scale using ImageJ (v1.8.0, NIH). After mild noise reduction, the outer or inner mitochondrial membrane is delineated as a 2-pixel-wide annular ROI that excludes cristae; an adjacent cytosolic area devoid of membranes serves as the background. Integrated optical density is extracted as the mean gray value of the membrane ROI minus the mean gray value of the background, yielding a background-corrected relative electron density. Normalization against the gray value of resin-only regions corrects for inter-batch variations. For each experimental condition, 10 mitochondria from 4 biological replicates were analyzed.

Assessment of intracellular reactive oxygen species (ROS) levels

MSCs at passage 2 were used for ROS assay. The determination of intracellular ROS levels was conducted using the Reactive Oxygen Species Assay Kit (Beyotime). The process began with the trypsinization of adherent cells, followed by thorough rinsing with a serum-free medium. Subsequently, the cells were labeled with 25 mM 2',7'-dichlorofluorescein diacetate and incubated at 37 °C for 30 min, with periodic gentle mixing every 5 min to ensure even labeling. After incubation, the cells were rinsed, collected, and reinfiltrate in PBS. The ROS levels were then visualized and quantified using a fluorescence microscope (Olympus Optical), capturing images of the stained adherent cells.

Alkaline phosphatase staining

For Alkaline phosphatase (ALP) staining, the MSCs were first rinsed with PBS (Gibco) and fixed with 4% paraformaldehyde (Beyotime) at 7 days post-induction. The ALP staining was conducted using a commercial kit (Beyotime) following the manufacturer's protocol. Briefly, cells were fixed with 4% PFA for 15 min, washed three times with PBS (Gibco), then incubated for 15 min at room temperature in freshly prepared BCIP/NBT working solution (3 mL Beyotime buffer A + 10 μL BCIP + 20 μL NBT). After three PBS (Gibco) rinses to stop the reaction, samples were harvested with ALP-positive regions appearing blue-purple. Images were captured, and the staining intensity was quantified using ImageJ software (v1.8.0, NIH).

Construction of cell-sheets

For the culture of cell-sheets, MSCs (passage 2) were evenly seeded at a density of 1×10^7 cells per well in 6-well plates (ThermoFisher Scientific), with each well containing 2 mL of α-MEM (Gibco) with 10% FBS (Gibco). Upon reaching confluence, the α-MEM medium (containing 10% FBS) was replaced with α-MEM (Gibco) supplemented with 10% FBS (Gibco) and 100 mg/mL ascorbic acid (Sigma-Aldrich) for an additional 10-day culture period. The medium was changed every 3 days to maintain optimal cell growth conditions. Over time, the white membrane became increasingly visible and the cell-sheet layer grew progressively thicker. The histological structure of the cell-sheet was tested via hematoxylin & eosin (H&E) staining.

Ectopic bone formation assay

A construct was created by layering four sheets of MSCs with three layers of hydroxyapatite/tricalcium phosphate (HA-TCP) (Sigma-Aldrich), with a total mass of 50 mg and a ratio of HA to TCP of 6:4, using particles sized between 50 and 200 nm, to form a sandwich-like structure. In brief, jawbone-derived MSCs from Control and BRONJ were harvested, and the BRONJ MSCs were pretreated with Fer-1 at a concentration of 10 μM (BRONJ + Fer-1). Then, a multilayered construct was engineered by alternately depositing MSCs-derived cell-sheets (Control, BRONJ, BRONJ + Fer-1) and HA-TCP granules (totally 50 mg) in a sandwich-like architecture: four consecutive cell-sheets interposed with three intervening HA-TCP layers, yielding a precisely stratified composite graft. Subsequently, the stratified sandwich was gently rolled into a cohesive, cylindrical mass to yield the definitive graft for subcutaneous implantation. Under general anesthesia induced by pentobarbital sodium (30 mg/kg), the cell-sheet/HA-TCP composites were implanted subcutaneously on the dorsal region of the nude mice. Eight weeks post-implantation, the mice were euthanized, and the implanted constructs were harvested for histological examination. The constructs were fixed in 4% paraformaldehyde (Beyotime) for 48 h and subsequently decalcified in 17% EDTA (Gibco) for two weeks. Once embedded in paraffin, the samples were sectioned and stained with H&E to assess tissue morphology. The regions of bone formation were visualized using biological microscope (Olympus Optical), and the images were analyzed using ImageJ software (v1.8.0, NIH). Quantitative assessments were performed on three randomly selected fields from each specimen to ensure accuracy and consistency in the evaluation of bone formation.

RNA extraction and quantitative real-time RT-PCR analysis of mRNA

Total RNA extraction was carried out using TRIzol reagent (Invitrogen, USA) in strict accordance with the manufacturer's protocol. One microgram of total RNA was reverse transcribed into complementary DNA (cDNA) utilizing a PrimeScript RT reagent kit (TaKaRa, Japan). Quantitative real-time RT-PCR analysis was conducted with the SYBR Premix Ex Taq II kit (TaKaRa) on a CFX96TM Real-Time RT-PCR System (Bio-Rad). β-actin served as the endogenous control for normalization of target mRNA levels. U6 served as the endogenous control for normalization of target microRNA levels. RUNX2 and OCN were tested seven days after osteogenic induction. The sequences of the primers employed for real-time RT-PCR are detailed in Supplementary Table S1.

Transfection of MSCs

For the transfection of MSCs (passage 2), the cells were initially plated into 6-well plates (ThermoFisher Scientific) with a density of 1×10^6, and the transfection process was initiated when the cells reached approximately 60% confluence. We used miR-145-3p mimics (chemically modified dsRNA (sense, 5'-GUCCAGUUU UCCCAGGAAUCCCU-3'; antisense with 2'-O-Me and

phosphorothioate linkages)), inhibitors (single-stranded 2'-O-methyl antagomir (5'-AGGGGAUUCCUGGGAA AACUGGAC-3', full PS backbone, 3'-Chol-TEG)), and a negative control (scrambled mimic and scrambled inhibitor with identical chemistry but non-targeting sequences) (all sourced from RiboBio, China), each diluted to a working concentration of 50 nM. The siPORT™ NeoFX™ Transfection Agent (Ambion, USA) was combined with diluted miR-145-3p reagents and allowed to form transfection complexes at room temperature for 10 min. These complexes consisted of 50 nM miRNA mimics or inhibitor plus 7.5 μL of the transfection agent per 1 mL of Opti-MEM (Gibco). Complexes were incubated 20 min at room temperature, then were subsequently overlayed onto the MSCs suspensions and incubated at 37 °C in α-MEM (Gibco) with 10% FBS (Gibco) for approximately 24 h. For verification of cargo loading, MSCs were harvested 24 h post-transfection. Total RNA isolated with TRIzol reagent (Invitrogen), miR-145-3p quantified by real-time qRT-PCR using U6 as endogenous control. The threshold for designation is a ≥ 50-fold increase for mimics or a ≥ 70% decrease for inhibitors, relative to their respective NC controls. Furthermore, MSCs were subjected to infection with IREB2 overexpression and silence lentivirus (RiboBio) at a titer of 1×10^8 TU/ml, supplemented with 5 μg/ml polybrene and complete medium (RiboBio). This incubation was carried out at 37 °C in α-MEM (Gibco) with 10% FBS (Gibco) for approximately 48 h.

Target prediction

We employed Targetscan version 8.0 to pinpoint potential targets of miR-145-3p. Our selection criteria for targets included those with a cumulative context score of ≤−0.5, as determined by Targetscan. In addition, we meticulously compiled a roster of iron metabolism-related targets, drawing from the comprehensive Genecards database, version 2024. With a commitment to the principle of evolutionary conservation, we further refined our preliminary screening to identify targets that exhibit high conservation across human, mouse, and rat species. Subsequently, we employed a Venn diagram to intersect the candidate targets derived from these three diverse sources, thereby elucidating the shared targets among them.

Luciferase reporter assay

Oligonucleotide sequences of IREB2 were amplified using specific primers designed with SpeI and HindIII restriction sites for subsequent cloning. The primer sequences were as follows: sense primer 5'- UUCUGUGCUGGA CCCAGGAAUCA-3' and anti-sense primer 5'- UUC UGUGCUGGACCCUCCUUAGA-3'. These sequences were inserted into the pMIR-Report luciferase plasmid (Ambion). For the assay, pMIR-control and pMIR-IREB2 plasmids served as the reporter constructs, while a Renilla luciferase reporter lacking miRNA binding sites was employed as an internal loading control. Co-transfection of all plasmids with miR-145-3p mimics, inhibitors, or negative controls into MSCs was achieved using Lipofectamine 2000 (Invitrogen). After a 48-hour incubation period, luciferase activities were quantified using a dual-luciferase reporter assay kit (Promega, USA), strictly adhering to the manufacturer's protocols. This approach allowed for the accurate measurement of reporter gene expression under the influence of miR-145-3p.

Engineered exosomes preparation, isolation and identity

MSCs (passage 2) were transfected with miR-145-3p mimics or inhibitor as mentioned above. After 48 h cultivation, MSCs were washed 3 times with PBS and cultured for another 48 h in 15 mL serum-free, vesicle-free α-MEM, which was refreshed once at 24 h. To eliminate residual cells from the harvested conditioned medium, the samples were centrifuged at 500 g for 10 min. The next step effectively removed cell debris and any apoptotic bodies, which were further cleared by a subsequent centrifugation of the supernatant at 16,000 g for 30 min. Subsequently, an ultracentrifugation step was performed to isolate the exosomes. This was carried out at 150,000 g for 70 min using a Beckman Optima XPN-100 ultracentrifuge (Beckman). The exosomes, once collected, were stored at −80 °C in PBS (Gibco) for future research applications.

The isolated exosomes were resuspended and stained with phosphotungstic acid (Sigma-Aldrich) to enhance their visibility under the electron microscope. The morphology of the exosomes was meticulously observed and their images were captured using a high-resolution TEM (Carl Zeiss). Subsequently, the isolated exosomes were characterized for their size and zeta potential using a dynamic light scattering and electrophoretic light scattering technique. The measurements were conducted on a Zetasizer Nano ZS (Malvern Instruments, UK). Prior to analysis, exosome suspensions were diluted in PBS (Gibco) to ensure optimal scattering conditions. The particle size distribution and zeta potential were determined by analyzing the Brownian motion of the exosomes, which provided insights into their stability and potential for cellular uptake. Additionally, the expression of specific exosomal proteins, TSG101 and CD63 (antibodies from Santa Cruz Biotechnology), was assessed as markers for exosome identity. The miR-145-3p expression in engineered exosomes was estimated using real-time RT-PCR.

BRONJ repair with exosome-enriched hydrogel

To treat BRONJ, we engineered an injectable scaffold by dispersing 1×10^{10} miR-145-3p-enriched exosomes into 250 μL of HyStem-HP hydrogel (Glycosan Biosystems, USA), yielding a final exosome density of 4×10^{10} particles/mL for targeted jawbone regeneration. Specifically, to fabricate an injectable HyStem-HP hydrogel incorporating therapeutic exosomes, the following standardized parameters were employed. A 1% (w/v) pre-polymer solution-comprising Glycosil, Heprasil and Gelin-S in the manufacturer-recommended ratio was prepared at 4°C. Purified MSCs-derived exosomes were introduced at a final concentration of 2 mg/mL ($\approx 4 \times 10^{10}$ particles/mL) and gently dispersed via three cycles of low-speed vortexing to minimize shear-induced membrane rupture. The mixture was immediately transferred to a 37 °C environment, where spontaneous oxidative cross-linking produced a robust hydrogel within 10 min without external light or enzymatic triggers.

To monitor the development of new bone tissue, calcein (8 mg/kg) (Sigma-Aldrich) was administered subcutaneously to all rats at 10-day and 3-day intervals preceding sacrifice. The regenerative capabilities of the MSCs were assessed through micro-CT scans using the Siemens Inveon scanner in Eschborn, Germany, adhering to a specific scanning protocol with a voltage of 80 kV, a current of 500 mA, and achieving an isotropic resolution of 14.97 mm. The Inveon Research Workplace 2.2 software by Siemens was employed for the analysis of new bone formation. Following the micro-CT scans, the jawbone underwent decalcification in 17% EDTA (Gibco), were embedded in paraffin, and sectioned coronally for H&E staining. The resulting regenerative junctions were documented using biological microscope with Olympus equipment, allowing for an evaluation of the quality and extent of bone regeneration.

Calcein labeling assay

Rats subjected to BRONJ and OVX-induced osteoporosis were administered calcein (8 mg/kg, Sigma) subcutaneously at intervals of 3 days and 10 days prior to euthanasia. The distal segments of the left femurs were harvested, fixed in 4% paraformaldehyde (Beyotime), and embedded in polymethyl methacrylate. The samples were sectioned into 50 μm slices, and the calcein labeling was visualized under a fluorescence microscope (Olympus Optical). The inter-calcein distance, indicative of the bone formation rate, was measured using ImageJ software (v1.8.0, NIH).

Co-culture of MSCs with exosomes

BRONJ-derived jawbone MSCs (passage 2) were seeded at 2×10^5 cells per well in 6-well plates (ThermoFisher Scientific) and allowed to attach for 12 h in α-MEM medium (Gibco) supplemented with 10% FBS (Gibco). Subsequently, the medium was refreshed with α-MEM (Gibco) plus 1% exosome-depleted FBS (Gibco) and 5×10^8 particles/mL of miR-145-3p-loaded exosomes. For evaluation of ferroptosis, MSCs were incubated with exosomes for 48 h at 37 °C with saturated humidity and 5% CO_2. The exosome-containing medium was removed and replaced with osteogenic induction medium composed of α-MEM (Gibco) supplemented with 10% FBS (Gibco), 5 mM β-glycerophosphate (Sigma-Aldrich), 50 μg/mL ascorbic acid (Sigma-Aldrich) and 10 nM dexamethasone (Sigma-Aldrich). MSCs were then maintained in this medium for 7 or 28 days before osteogenic gene expression was analyzed by real-time qPCR and matrix mineralization was assessed by Alizarin Red S staining.

Immunofluorescence staining assay

The MSCs (passage 2) were fixed and rinsed, followed by treatment with 0.2% Triton X-100 (Sigma-Aldrich) to permeabilize the cell membranes. After another round of rinsing, the cells were incubated with the primary antibody specific to rat osteocalcin (OCN) (Santa Cruz Biotechnology) for 12 h at 4 °C. Subsequence to rinsing, the cells were incubated with a fluorescent secondary antibody (Santa Cruz Biotechnology) at room temperature for 2 h to enable visualization of the antigen-antibody complexes. The cell nuclei were then counterstained with Hoechst 33,342 (Sigma-Aldrich) for 10 min at room temperature to facilitate nuclear identification. The stained cells were examined using a fluorescence microscope (Olympus Optical). Both original and merged images were captured and processed using the DP controller or DP manager software (Olympus Optical). Immunofluorescence intensity was quantified using ImageJ software (v1.8.0, NIH).

Immunohistochemical staining assay

The subcutaneous grafts were harvested seven days after transplantation. The paraffin-embedded subcutaneous graft sections underwent dewaxing and hydration processes. To inhibit endogenous peroxidase activity, the sections were treated with 3% hydrogen peroxide (MKbio, China) for 15 min at room temperature. Following this, the sections were rinsed with PBS (Gibco) and then incubated with a blocking buffer (Beyotime) for one hour to prevent non-specific binding. The slides were subsequently incubated with a primary anti-OCN antibody (Santa Cruz Biotechnology) (diluted at 1:200) for 12 h at 4 °C. After thorough washing, the slides were further incubated with a biotinylated secondary antibody (Boster) (also diluted at 1:200) for one hour at 37 °C. This was followed by incubation with an HRP-streptavidin complex for 30 min. The slides were then developed using the DAB chromogen kit (Gene Tech, USA) until light brown staining became visible, indicating successful

antigen detection. Quantitative analysis of immunohistochemical positive areas was performed with ImageJ software (v1.8.0, NIH).

Systemic injection of MSCs for osteoporosis treatment

A cohort of twenty 8-week-old SD rats was randomly and evenly allocated to four groups: Normal, Osteoporosis (OP), OP + BRONJ MSCs, and OP + reprogrammed MSCs. Under general anesthesia, the Normal group underwent a sham operation involving the resection of a small amount of fat near the ovaries, while the other groups underwent bilateral ovariectomy. Twenty-four hours postoperatively, rats in the OP + BRONJ MSCs and OP + reprogrammed MSCs groups were systemically injected via the tail vein with MSCs (passage 2) derived from the jawbone before and after BRONJ therapy, respectively, at a dosage of 2×10^7 cells/kg. Rats in the Normal and OP groups received an equivalent volume of PBS (Gibco). To track new bone formation, calcein (8 mg/kg, Sigma-Aldrich) was administered subcutaneously to all rats 10 days and 3 days prior to sacrifice. Ten weeks after the surgical procedures, both femurs were harvested post-mortem and fixed in 4% paraformaldehyde (Beyotime). The left femurs were reserved for hard tissue sectioning to assess calcein labeling. The right femurs underwent micro-CT analysis (General Electric Company, USA) following a standardized scanning protocol, which included a voltage of 80 kV, a current of 80 μA, and an isotropic resolution of 14 mm. Bone volume to total volume ratio (BV/TV) and trabecular bone parameters were calculated using the system's integrated software (General Electric Company). Following micro-CT analysis, the right femurs were decalcified, embedded, and sectioned for H&E staining in accordance with standard protocols.

Critical-sized calvarial defects repair assay

A group of ten 8-week-old SD rats was randomly and equally assigned to two experimental groups: Defect + BRONJ MSCs and Defect + reprogrammed MSCs. Under general anesthesia, a circular critical-sized defect measuring 8 mm in diameter was created in the central region of the calvarium. To address this defect, a composite scaffold was engineered by layering four sheets of MSCs (passage 2) with three layers of hydroxyapatite/tricalcium phosphate (HA-TCP) (Sigma-Aldrich), totaling 50 mg, to form a sandwich structure designed for calvarial defect repair. Twelve weeks post-transplantation, all rats were euthanized, and their skulls were fixed in 4% paraformaldehyde (Beyotime). The reparative efficacy of the MSCs was evaluated using micro-CT (Siemens Inveon, Eschborn, Germany) according to a specific scanning protocol, which included a voltage of 80 kV, a current of 500 mA, and an isotropic resolution of 14.97 mm. Analysis of new bone formation was conducted using Inveon Research Workplace 2.2 software (Siemens Inveon Eschborn). Following micro-CT scanning, the skulls were decalcified with 17% EDTA (Gibco), embedded in paraffin, and sectioned in the coronal plane for H&E staining. The regenerative junctions were then photographed using biological microscope (Olympus Optical) to assess the quality and extent of bone regeneration.

Statistical analysis

Data are presented as mean ± standard deviation (S.D.). Prior to statistical analysis, data underwent normality and homogeneity of variance tests. Comparisons were conducted using Student's t-test between two groups; One-way analysis of variance (ANOVA) with Tukey's post hoc test was used for multiple group comparisons. Statistical analysis and charts were performed by GraphPad Prism 9.0.0 (GraphPad Software, USA). Significance was set at the $p < 0.05$ threshold.

Results

BRONJ disrupts ferroptotic homeostasis in jawbone-resident MSCs

This segment endeavored to explore the impact of BRONJ on ferroptosis within MSCs harvested from the jawbone. First, jawbone MSCs were isolated and cultured from both control and BRONJ rats. Immunophenotypic characterization revealed that both cell populations were uniformly positive for CD29 and CD90, while negative for CD45 (Figure S1A and B). Furthermore, each population exhibited clonogenic potential (Figure S1C and D) and retained the capacity for osteogenic (Figure S1E and F) and adipogenic differentiation (Figure S1G and H), thereby confirming their authentic MSCs identity. Figure 1 A illustrates a contrast between the control group, which maintained a robust cell survival rate of nearly 100%, and the BRONJ group, which experienced a sharp decline in cell survival, leaving fewer than 40% of cells retaining viability. This marked reduction in cell survival underscores the cytotoxic effects intrinsic to BRONJ.

Comparative analysis revealed that the BRONJ group had significantly higher iron levels than the control group, as depicted in Fig. 1B. This elevation reflects the disrupted iron homeostasis and increased iron accumulation that are hallmarks of BRONJ. Additionally, the BRONJ group exhibited markedly higher levels of MDA, a biomarker indicative of lipid peroxidation during ferroptosis, as shown in Fig. 1C. A significant reduction in GPX4 expression, a cellular signature of ferroptosis, was observed in jawbone MSCs from BRONJ rats when compared to the control group, as indicated in Fig. 1D and E. Assessment of mitochondrial morphology (Fig. 1 F), a pivotal factor in ferroptosis, revealed that while the control group displayed normal mitochondrial size and

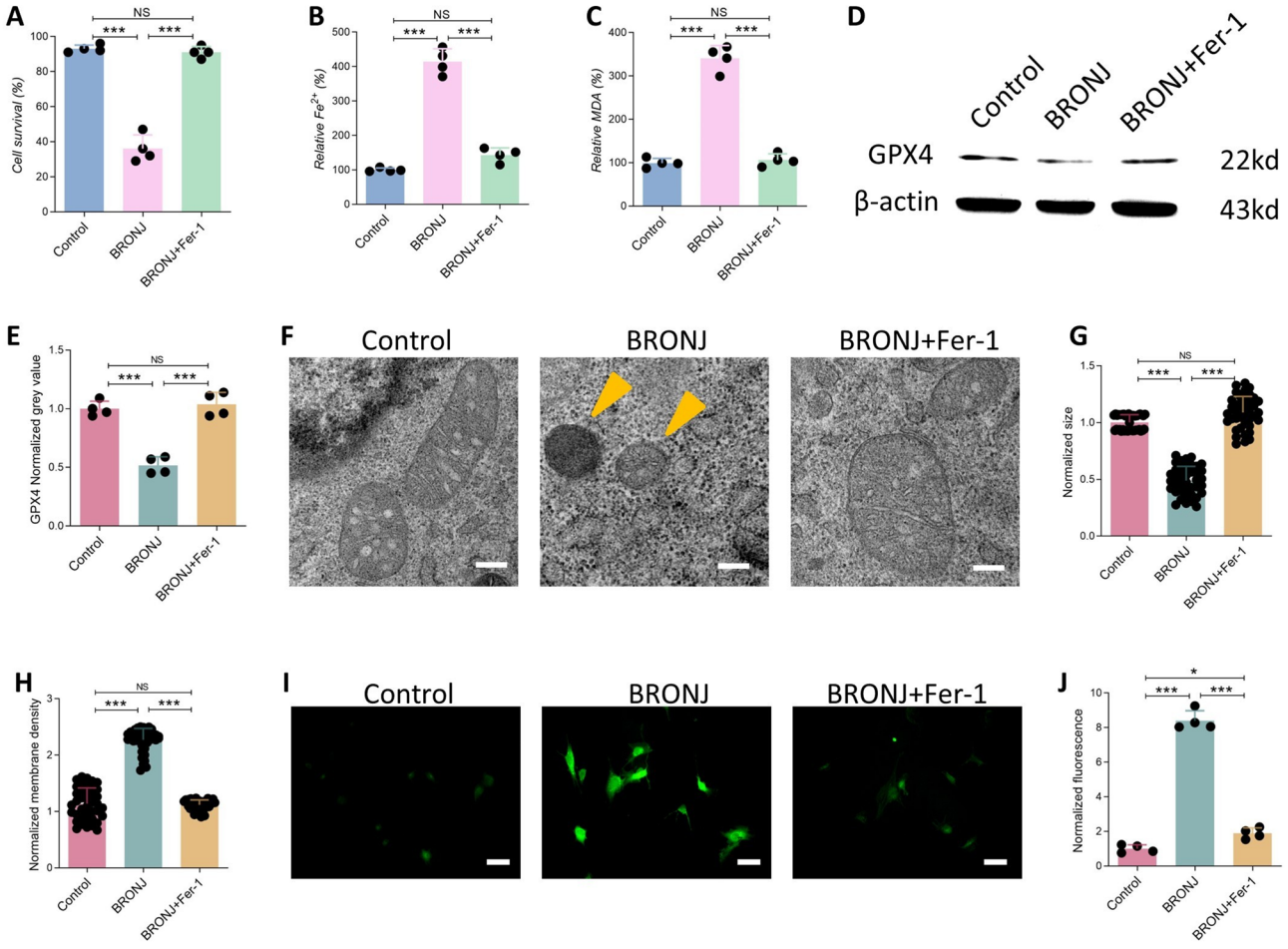

Fig. 1 BRONJ Triggers Ferroptotic Perturbation in Jawbone MSCs. (**A**) Cell survival, (**B**) Relative Fe^{2+} level, (**C**) MDA level, (**D**) GPX4 protein expression and its (**E**) quantification of jawbone MSCs in group of Control, BRONJ and BRONJ + Fer-1. (**F**) The mitochondrial morphology in MSCs was captured using TEM. Scale bar, 0.5 μm. (**G**) The size and (**H**) membrane density of mitochondria in MSCs were determined from TEM micrographs using ImageJ software. (**I**) Immunofluorescence staining of ROS level and (**J**) its quantitative analysis in MSCs. Scale bar, 20 μm. Data are presented as means ± SD ($n = 4$; ten mitochondria were examined per sample, yielding a total of 40 mitochondria per group). *$p < 0.05$; **$p < 0.01$; ***$p < 0.001$

membrane density, the BRONJ group showed evidence of mitochondrial contraction and increased mitochondrial membrane density (Figs. 1G and H), suggesting mitochondrial dysfunction. Furthermore, ROS levels, a critical bioindicator of oxidative stress during ferroptosis, were significantly higher in the BRONJ group than in the control group, as illustrated in Fig. 1I and J. Collectively, these findings indicate that ferroptosis in jawbone MSCs of BRONJ rats is abnormally elevated.

The administration of Fer-1, a potent inhibitor of ferroptosis, to the BRONJ group resulted in a remarkable improvement in cell survival (Fig. 1A), along with a reduction in iron and MDA levels (Fig. 1B C), respectively. Additionally, GPX4 levels were elevated (Fig. 1D and E), mitochondrial morphology (Fig. 1F), size (Fig. 1G) and membrane density (Fig. 1H) were ameliorated, and ROS levels (Fig. 1I and J) were diminished. These observations underscore the significant role of ferroptosis in BRONJ-affected jawbone MSCs.

Ferroptosis triggers osteogenic dysfunction in jawbone-derived MSCs affected with BRONJ

Our subsequent investigation focused on the effects of BRONJ and ferroptosis on the osteogenic differentiation potential of MSCs derived from the jawbone. Jawbone MSCs from BRONJ rats exhibited the same surface-marker profile as control cells (Figure S1A and B). However, their clonogenic capacity (Figure S1C and D) and osteogenic potential (Figure S1E and F) were significantly reduced, whereas their adipogenic potential was markedly enhanced (Figure S1G and H). This observation indicates that, even though the surface immunophenotype of MSCs remains intact, their functional differentiation potential can still be reprogrammed within the BRONJ microenvironment.

ALP activity, an early indicator of osteogenic differentiation, was evaluated as shown in Fig. 2A and B. The control group displayed substantial ALP activity, indicating intact osteogenic function. Conversely, the BRONJ

group exhibited a notable decrease in ALP activity, suggesting an impediment in osteogenic differentiation capacity. The mineralization of the extracellular matrix, a late-stage indicator of osteogenic differentiation, was assessed using Alizarin Red S staining, as depicted in Fig. 2C and D. The control group presented a high level of mineralization, evident from the intense red staining. In contrast, the BRONJ group demonstrated a significant reduction in Alizarin Red S staining, indicating a diminished mineralization capacity. Cell-sheet/HA-TCP "sandwich" constructs (Figure S2A and B) were subcutaneously implanted into nude mice to assess their in vivo ectopic osteogenic capacity (Fig. 2E and F). The control group exhibited substantial new bone formation, as indicated by normalized new bone formation values. The BRONJ group, however, showed a marked reduction in new bone formation, aligning with the in vitro observations of compromised osteogenic differentiation. The expression of key osteogenic genes, RUNX2 and OCN, was further evaluated to elucidate the molecular mechanisms affected by BRONJ, as shown in Fig. 2G and H. The control group exhibited high expression levels of both RUNX2 and OCN, consistent with active osteogenic differentiation. In contrast, the BRONJ group showed significant downregulation of these genes, correlating with the observed reduction in osteogenic differentiation markers.

An in vitro concentration-response screen identified 10 nM as the optimal Fer-1 treatment concentration (Figure S3A-C). Treatment with Fer-1 in the BRONJ + Fer-1 group resulted in a recovery of ALP activity, as seen in Fig. 2A and B, and a significant enhancement in the mineralization process in BRONJ-affected MSCs in vitro, as indicated in Fig. 2C and D. Notably, the BRONJ + Fer-1 group also displayed a marked increase in new bone formation in vivo (Fig. 2E and F) and an upregulation of RUNX2 and OCN (Fig. 2G and H). Collectively, these findings demonstrate that ferroptosis negatively regulates the osteogenic differentiation ability of jawbone MSCs in BRONJ-affected rats.

MiR-145-3p governs ferroptosis and lineage commitment in jawbone MSCs compromised by BRONJ

To clarify the role of miR-145-3p in modulating ferroptosis in MSCs from the jawbone in BRONJ rats, we concentrated on the expression of miR-145-3p and its impact on ferroptosis following both overexpression and knockdown. Our analysis disclosed a marked reduction of miR-145-3p expression in BRONJ-impacted MSCs relative to the control group, as depicted in Fig. 3A. This diminished expression of miR-145-3p implies its potential role in the pathophysiology of BRONJ. The use of mimics and inhibitors enabled us to modulate miR-145-3p expression (Fig. 3B).

Investigating the functional role of miR-145-3p in ferroptosis, we observed that overexpression of miR-145-3p (BRONJ + Mimics) led to a substantial reduction in ferroptosis, characterized by enhanced cell survival (Fig. 3C), diminished levels of iron (Fig. 3D) and MDA (Fig. 3E). Moreover, overexpression of miR-145-3p resulted in elevated GPX4 expression (Fig. 3F and G), and mitigated mitochondrial contraction (Fig. 3H and I) along with reduced mitochondrial membrane density (Fig. 3H and J), indicating an amelioration in mitochondrial function. A decrease in oxidative stress was also noted after miR-145-3p overexpression, as illustrated in Fig. 3K and L.

In contrast, the knockdown of miR-145-3p (BRONJ + Inhibitor) resulted in a decrease in cell survival (Fig. 3M), an increase in iron (Fig. 3N) and MDA levels (Fig. 3O). It also led to a reduction in GPX4 expression (Fig. 3P and Q), an exacerbation of mitochondrial contraction (Fig. 3R and S) and mitochondrial membrane density (Fig. 3R and T), accompanied by an increase in oxidative stress, as demonstrated in Fig. 3U and V.

The miR-145-3p/IREB2 axis orchestrates ferroptotic homeostasis and osteogenic commitment in jawbone-derived MSCs from BRONJ

To investigate the role of miR-145-3p in the osteogenic differentiation of ferroptotic MSCs from the jawbone, we identified IREB2 as a key target, a molecule significantly involved in iron metabolism, using target prediction analysis (Figure S4A and B), luciferase assays (Figure S4C), IREB2 gene (Figure S4D) and protein expression (Figure S4E and F) analysis. Our initial findings confirmed no difference in IREB2 gene expression across control, BRONJ, and BRONJ + Fer-1 groups (Fig. 4A). However, IREB2 protein expression was elevated in BRONJ-affected MSCs, and the inhibition of ferroptosis led to a reduction in IREB2 protein levels (Fig. 4B and C). This suggests that IREB2 is associated with BRONJ and may be modulated post-translationally.

Further, we established the influence of miR-145-3p modulation on ferroptosis and osteogenic differentiation through the regulation of IREB2. Overexpression of miR-145-3p (Mimics + IREB2) resulted in a significant decrease in cell survival (Fig. 4D), an increase in iron (Fig. 4E) and MDA levels (Fig. 4F) compared to the Mimics + Vector group. To evaluate the functional outcomes of miR-145-3p and IREB2 modulation on osteogenic differentiation, we examined osteogenic gene expression, in vitro mineralization, and in vivo bone formation. Our data indicated that the addition of IREB2 neutralized the effects of miR-145-3p overexpression on enhanced RUNX2 (Fig. 4G), OCN (Fig. 4H), in vitro mineralization (Fig. 4I and J), and in vivo bone formation (Fig. 4K and L).

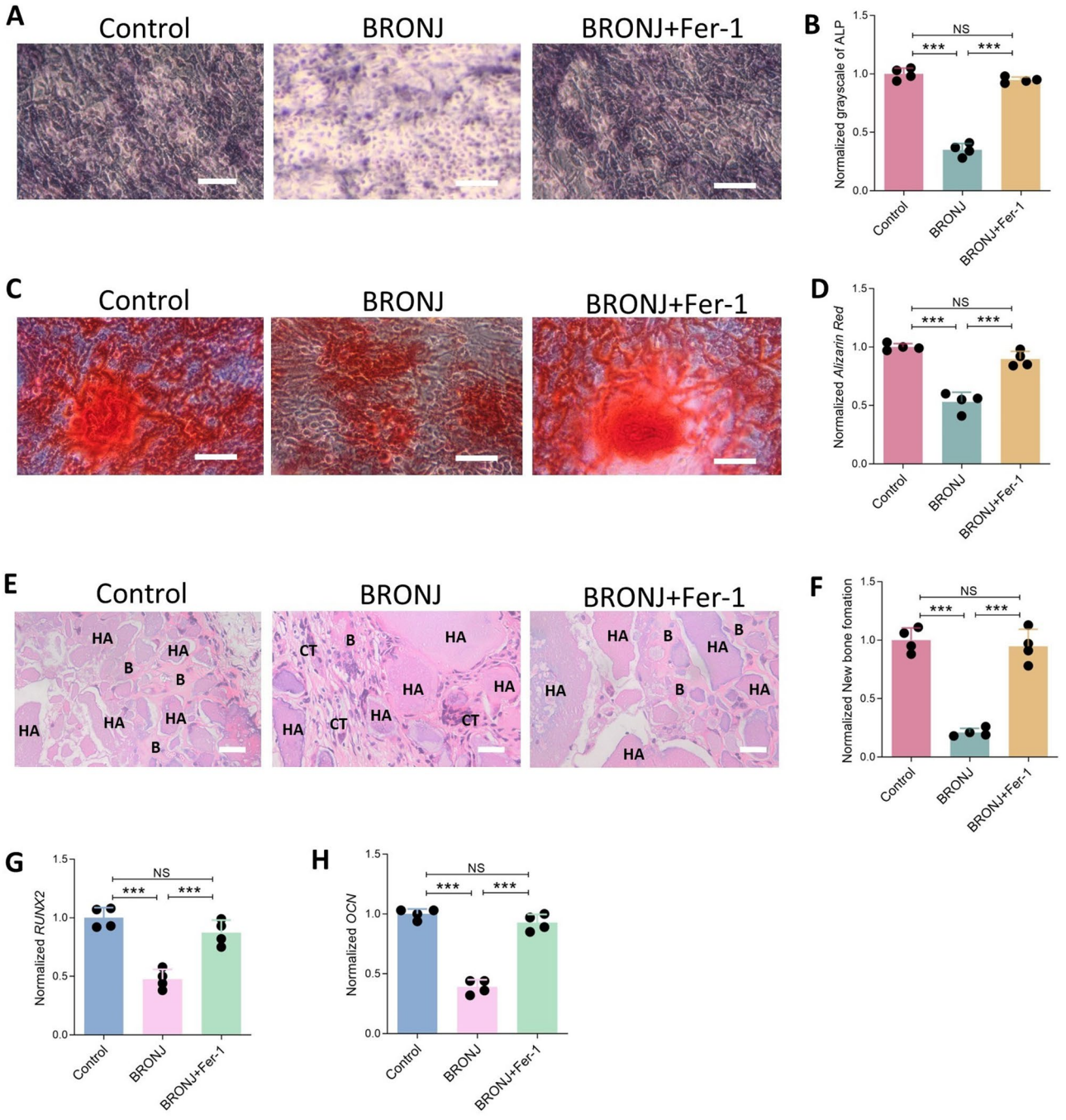

Fig. 2 Ferroptosis-Driven Erosion of Osteogenic Competence in Jawbone MSCs under BRONJ Conditions. (**A**) ALP staining of MSCs and its (**B**) quantitative analysis. (**C**) Mineralized nodules formation of MSCs and its (**D**) quantitative analysis. Scale bar, 20 μm. (**E**) H&E staining of subcutaneous ectopic ossification induced by MSCs transplantation in nude mice (HA: HA-TCP, B: new bone, CT: connective tissue) and its (**F**) quantitative analysis. Scale bar, 50 μm. (**G**) Normalized RUNX2 and (**H**) OCN gene expressions in MSCs. Data are presented as means ± SD ($n = 4$). *$p < 0.05$; **$p < 0.01$; ***$p < 0.001$

Conversely, the knockdown of IREB2 mitigated the negative effects of miR-145-3p inhibitor on cell survival (Fig. 4M), iron (Fig. 4N) and MDA levels (Fig. 4O), as well as on RUNX2 (Fig. 4P), OCN (Fig. 4Q), in vitro mineralization (Fig. 4R and S), and in vivo bone formation (Fig. 4T and U). These results underscore the pivotal role of the miR-145-3p/IREB2 signaling pathway in regulating ferroptosis and, consequently, the osteogenic differentiation of jawbone MSCs in BRONJ rats.

Exosome-delivered miR-145-3p potentiates osteogenic reconstitution and accelerates bone repair in BRONJ

This section explores the effects of exosome-mediated miR-145-3p modulation on ferroptosis, and provides

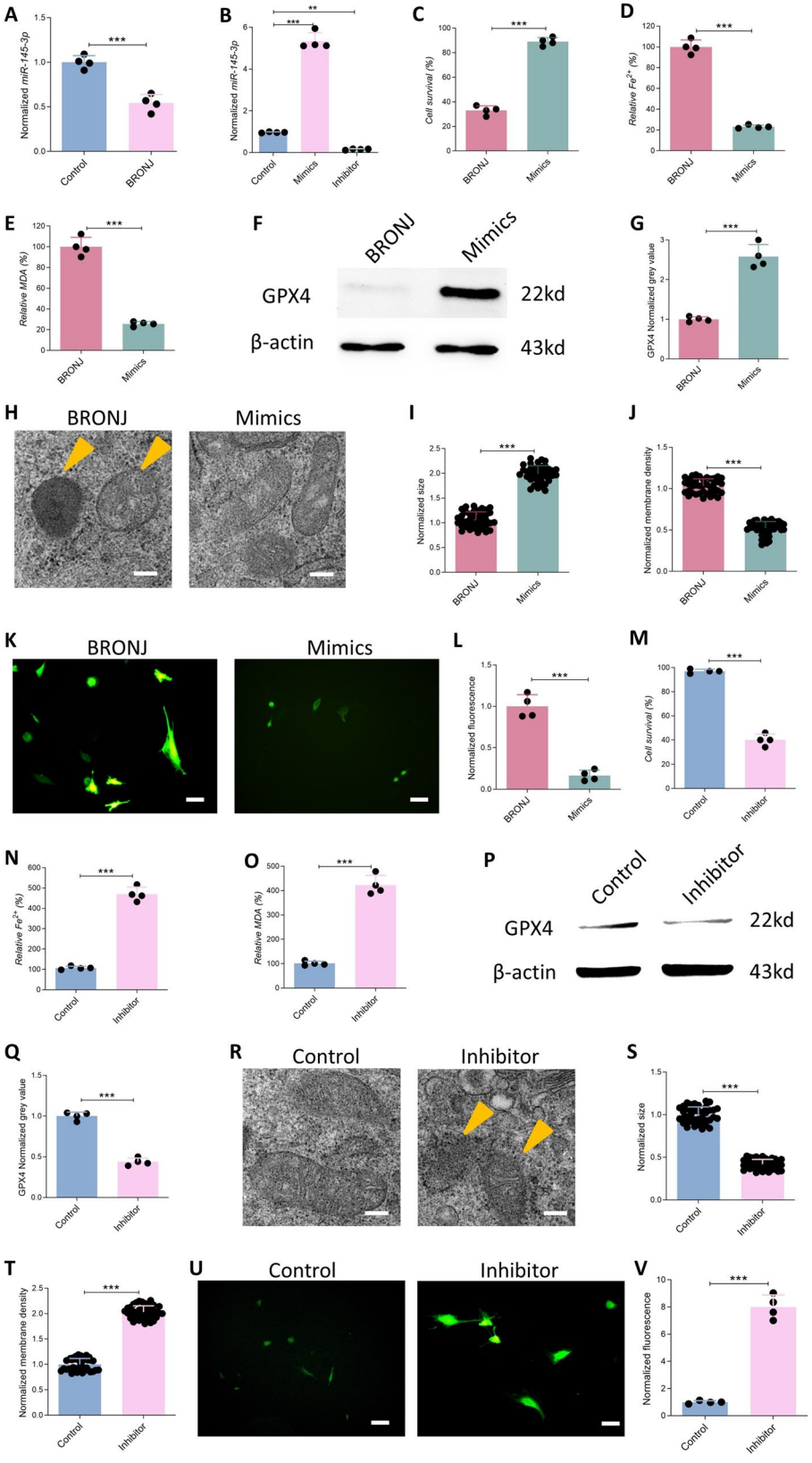

Fig. 3 (See legend on next page.)

(See figure on previous page.)

Fig. 3 miR-145-3p Orchestrates Ferroptotic Signaling and Lineage Commitment in BRONJ-Derived MSCs. (**A**) Normalized miR-145-3p expressions in Control and BRONJ MSCs. (**B**) Normalized miR-145-3p expressions in MSCs treated with vector, mimics and inhibitor. (**C**) Cell survival, (**D**) Relative Fe^{2+} level, (**E**) MDA level, (**F**) GPX4 expression and its (**G**) quantification of BRONJ jawbone MSCs treated with vector and mimics. (**H**) The mitochondrial morphology in BRONJ MSCs treated with vector and mimics. Scale bar, 0.5 μm. (**I**) The size and (**J**) membrane density of mitochondria in BRONJ MSCs treated with vector and mimics were determined from TEM micrographs using ImageJ software. (**K**) Immunofluorescence staining and its (**L**) quantitative analysis of ROS level in BRONJ MSCs treated with vector and mimics. Scale bar, 20 μm. (**M**) Cell survival, (**N**) Relative Fe^{2+} level, (**O**) MDA level, (**P**) GPX4 expression and its (**Q**) quantification of Control MSCs treated with vector and inhibitor. (**R**) The mitochondrial morphology in Control MSCs treated with vector and inhibitor. Scale bar, 0.5 μm. (**S**) The size and (**T**) membrane density of mitochondria in Control MSCs treated with vector and inhibitor were determined from TEM micrographs using ImageJ software. (**U**) Immunofluorescence staining and its (**V**) quantitative analysis of ROS level in Control MSCs treated with vector and inhibitor. Scale bar, 20 μm. Data are presented as means ± SD ($n = 4$; ten mitochondria were examined per sample, yielding a total of 40 mitochondria per group). $^{*}p < 0.05$; $^{**}p < 0.01$; $^{***}p < 0.001$

a detailed analysis of the in vivo therapeutic efficacy of miR-145-3p modulation in BRONJ through the transplantation of engineered exosomes. First, exosomes were isolated from jawbone MSCs and comprehensively characterized by morphology (Figure S5A), particle size (Figure S5B), zeta potential (Figure S5C), and the canonical exosomal markers TSG101 and CD63 (Figure S5D). Figures 5A depict the expression levels of miR-145-3p and the extent of ferroptosis in endogenous MSCs following the transplantation of exosomes-loaded hydrogel that either overexpress or knockdown miR-145-3p. The findings indicate that the transplantation of exosomes overexpressing miR-145-3p led to a significant increase in miR-145-3p levels within endogenous MSCs (Fig. 5 A), whereas the transplantation of exosomes knocking down miR-145-3p resulted in a decrease (Fig. 5 A). This adjustment in miR-145-3p expression influenced ferroptosis levels, as reflected by alterations in cell survival (Fig. 5B), iron levels (Fig. 5 C) and MDA levels (Fig. 5D). Consistent with the in vivo findings, co-culture of BRONJ MSCs with miR-145-3p-enriched exosomes in vitro markedly elevated intracellular miR-145-3p levels (Figure S6A), concomitantly ameliorating indices of ferroptosis, including cell survival (Figure S6B), iron (Figure S6C) and MDA accumulation (Figure S6D).

Figures 5E-I display the microCT analysis and bone parameters of the jawbone necrosis area following exosomes transplantation. The data reveal that exosomes overexpressing miR-145-3p (BRONJ + exo-up-miR) significantly enhanced new bone formation, as illustrated in Fig. 5E, and improved key bone parameters, including bone volume to total volume ratio (BV/TV) (Fig. 5 F), trabecular thickness (Fig. 5G), trabecular number (Fig. 5H), and reduced trabecular spacing (Fig. 5I). In contrast, the knockdown of miR-145-3p (Control + exo-down-miR) exerted adverse effects on these parameters (Fig. 5E-I). H&E staining of BRONJ lesions, as shown in Fig. 5 J, highlighted distinct differences in tissue morphology among the control, BRONJ, and exosome-treated groups. The control group exhibited healthy bone tissue, whereas the BRONJ group displayed characteristics of necrosis and diminished bone quality. Notably, treatment with exosomes overexpressing miR-145-3p led to improved tissue morphology, suggesting a therapeutic benefit.

To assess in vivo osteogenesis, calcein staining and quantification of the osteogenic rate were employed. The findings indicate that exosomal overexpression of miR-145-3p enhanced new bone formation, as evidenced by augmented calcein deposition (Fig. 5 K) and an elevated osteogenic rate (Fig. 5L). Conversely, the knockdown of miR-145-3p negatively impacted these osteogenic processes, as exhibited in Fig. 5 K and L. These results underscore the potential of engineered exosomes containing miR-145-3p as a therapeutic strategy for BRONJ.

Exosome-shuttled miR-145-3p suppresses ferroptotic stress and restores the osteogenic competence of resident MSCs in BRONJ

This section explores the effects of exosome-mediated miR-145-3p modulation on osteogenic differentiation in endogenous MSCs within the BRONJ context. It reveals that the overexpression of miR-145-3p in exosomes significantly enhances ALP activity (Fig. 6 A and B) and mineralization (Fig. 6 C and D) of endogenous MSCs after the transplantation of exosomes modulating miR-145-3p, signs of improved osteogenic differentiation. Conversely, the knockdown of miR-145-3p diminishes these parameters (Fig. 6A-D). Immunofluorescence staining for OCN, a late-stage osteogenic differentiation marker, is presented in Fig. 6E, with quantitative analysis provided in Fig. 6F. The results demonstrate that the overexpression of miR-145-3p in exosomes improves OCN expression, while its knockdown results in a decrease, further confirming the role of miR-145-3p in facilitating osteogenic differentiation.

H&E staining of ectopic bone formation is shown in Fig. 6G, with the quantitative analysis of new bone formation presented in Fig. 6H. The data demonstrate that exosomal overexpression of miR-145-3p enhances the osteogenic capacity of BRONJ-derived MSCs thereby facilitating new bone formation, whereas its knockdown suppresses these processes. Immunohistochemistry staining for OCN in ectopic bone formation is depicted in Fig. 6I, with quantitative analysis provided in Fig. 6J. Consistent with the immunofluorescence staining, these

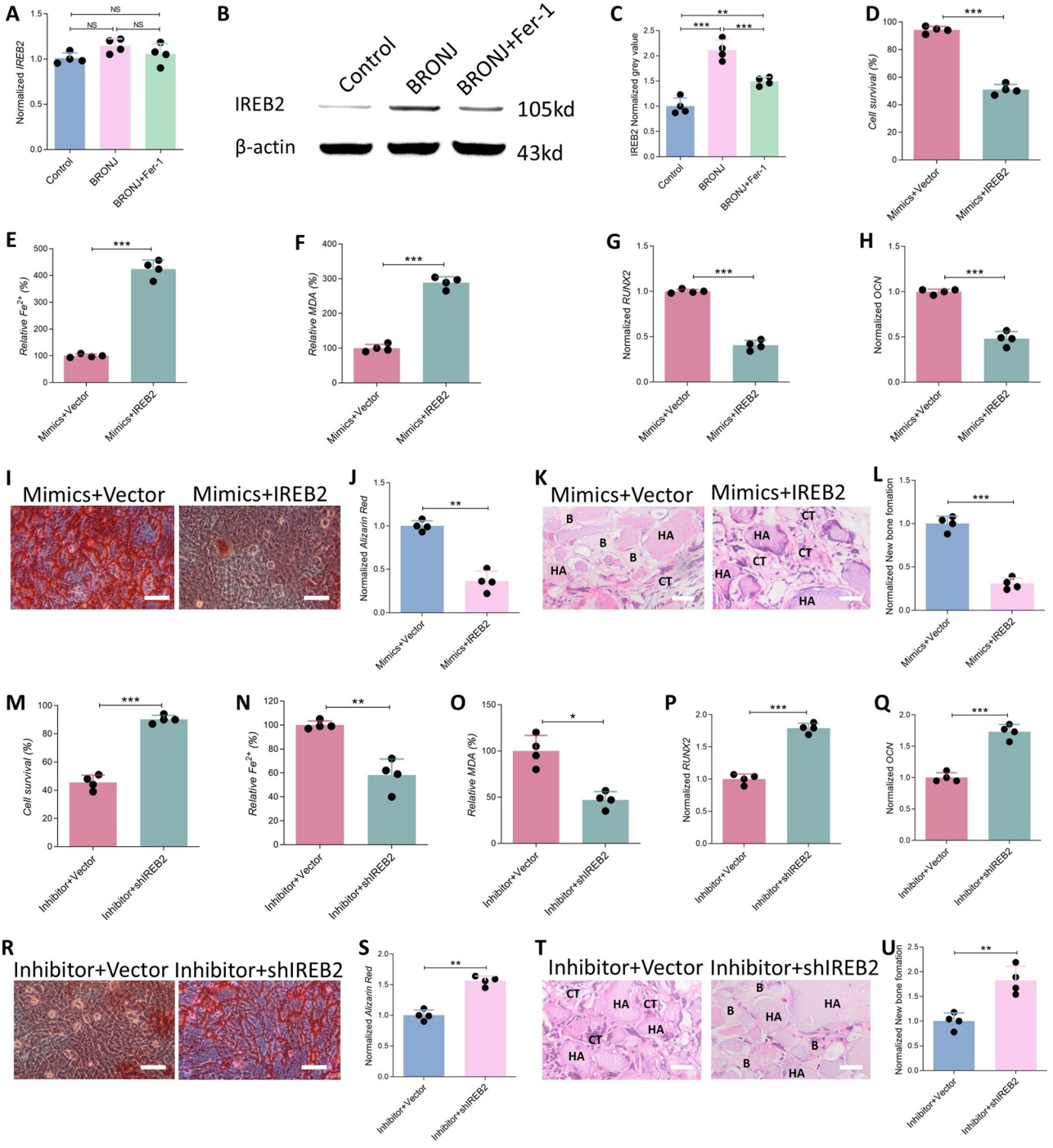

Fig. 4 The miR-145-3p/IREB2 Axis Governs Ferroptosis and Osteogenic Lineage Specification in Jawbone MSCs Isolated from BRONJ Lesions. (**A**) Normalized IREB2 gene, (**B**) protein expressions and (**C**) the quantification in jawbone MSCs of Control group, BRONJ group and BRONJ + Fer-1 group. (**D**) Cell survival, (**E**) Relative Fe^{2+} level and (**F**) MDA level in jawbone MSCs of mimics + vector group and mimics + IREB2 group. (**G**) Normalized RUNX2 and (**H**) OCN gene expressions, (**I**) Mineralized nodules formation and its (**J**) quantitative analysis in jawbone MSCs of mimics + vector group and mimics + IREB2 group. Scale bar, 20 μm. (**K**) H&E staining of subcutaneous ectopic ossification induced by MSCs transplantation and (**L**) the quantification in mimics + vector group and mimics + IREB2 group (HA: HA-TCP, B: new bone, CT: connective tissue). Scale bar, 50 μm. (**M**) Cell survival, (**N**) Relative Fe^{2+} level and (**O**) MDA level in jawbone MSCs of inhibitor + vector group and inhibitor + shIREB2 group. (**P**) Normalized RUNX2 and (**Q**) OCN gene expressions, (**R**) Mineralized nodules formation and its (**S**) quantitative analysis in jawbone MSCs of inhibitor + vector group and inhibitor + shIREB2 group. Scale bar, 50 μm. (**T**) H&E staining of subcutaneous ectopic ossification induced by MSCs transplantation and (**U**) the quantification in inhibitor + vector group and inhibito + shIREB2 group (HA: HA-TCP, B: new bone, CT: connective tissue). Scale bar, 200 μm. Data are presented as means ± SD ($n = 4$). *$p < 0.05$; **$p < 0.01$; ***$p < 0.001$

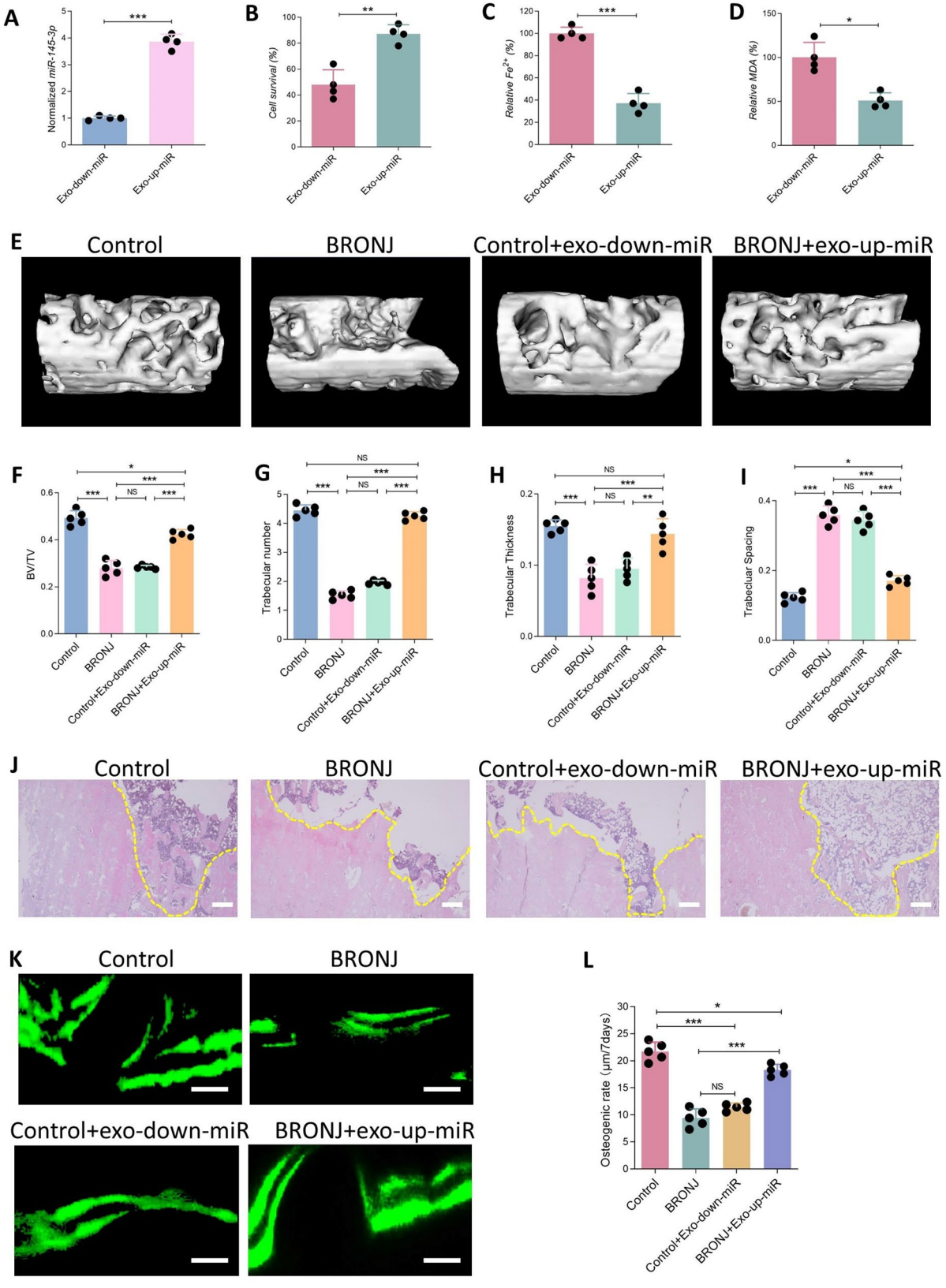

Fig. 5 (See legend on next page.)

(See figure on previous page.)

Fig. 5 Exosome-Delivered miR-145-3p Potentiates Osseous Regeneration in BRONJ Lesions via Robust In Vivo Efficacy. (**A**) Normalized miR-145-3p expressions in exosomes derived from MSCs treated with inhibitor and mimics. (**B**) Cell survival, (**C**) Relative Fe^{2+} level and (**D**) MDA level of BRONJ jawbone MSCs treated with exo-down-miR and exo-up-miR. (**E**) The 3D morphology, (**F**) BV/TV, (**G**)Trabecular number, (**H**)Trabecular thickness and (**I**)Trabecular space of the osteonecrotic jawbone in Control group, BRONJ group, BRONJ + exo-down-miR group and BRONJ + exo-up-miR group. (**J**) H&E staining of osteonecrotic jawbone in Control group, BRONJ group, BRONJ + exo-down-miR group and BRONJ + exo-up-miR group. Scale bar, 200 μm. (**K**) Calcein labeling and its (**L**) quantitative analysis of osteonecrotic jawbone in Control group, BRONJ group, BRONJ + exo-down-miR group and BRONJ + exo-up-miR group. Scale bar, 50 μm. Data are presented as means ± SD ($n = 5$). *$p < 0.05$; **$p < 0.01$; ***$p < 0.001$

results show that the overexpression of miR-145-3p in exosomes increases OCN expression and subsequent bone formation, while the knockdown of miR-145-3p reduces these parameters. In line with the in vivo observations, in vitro co-culture of BRONJ-affected MSCs with miR-145-3p-enriched exosomes substantially restored their osteogenic capacity (Figure S6E and F), as evidenced by markedly elevated expression of the osteogenic regulators RUNX2 and OCN (Figure S6G and H).

Exosome-reprogrammed BRONJ-derived MSCs restore osteogenesis in osteogenesis-impaired skeletal disorders

Following exosome-mediated rescue of BRONJ, we harvested reprogrammed jawbone MSCs (After exosome-mediated transfer of miR-145-3p, the post-necrotic microenvironment is reprogrammed: miR-145-3p concurrently represses ferroptotic signaling and amplifies osteogenic transcriptional programs in resident MSCs, thereby converting them into a rejuvenated, lineage-competent population that we operationally term "reprogrammed MSCs.") from the treated rats. Transplantation with miR-145-3p-enriched exosomes elevated intracellular miR-145-3p levels in BRONJ-derived jawbone MSCs (Figure S7A) and concomitantly increased the miR-145-3p cargo of their secreted exosomes (Figure S7B), indicating that these reprogrammed MSCs may possess the potential to serve as vehicles for miR-145-3p delivery in skeletal disorders. These endogenous MSCs were isolated, expanded and then transplanted into two in vivo models that are associated with ferroptosis and osteogenic impairment: an OVX-induced osteoporosis model and a critical-sized calvarial defect model (Figure S8). Through quantitative micro-CT and dynamic histomorphometry, we investigate the intrinsic osteogenic capacity of the endogenous MSCs pool to determine whether exosome therapy effectively restores their competence for new bone formation under osteogenesis-impaired conditions. Figures 7A present high-resolution micro-CT reconstructions and quantitative bone-morphometric analyses of femurs from osteoporotic rats administered reprogrammed MSCs derived from treated BRONJ rats. Post-transplantation with exo-up-miR, the endogenous MSCs harvested from BRONJ-affected jawbones (reprogrammed MSCs) demonstrated a significant capacity to mitigate osteoporosis, as shown in Fig. 7A. This improvement was marked by enhanced BV/TV (Fig. 7B), trabecular number (Fig. 7 C), trabecular thickness (Fig. 7D), and reduced trabecular spacing (Fig. 7E) when compared to both the Osteoporosis group and the OP + BRONJ MSCs group. H&E staining of femurs, as depicted in Fig. 7 F, revealed that the bone mass in the OP + reprogrammed MSCs group was superior to that of the Osteoporosis group and the OP + BRONJ MSCs group. Figures 7G and H display calcein fluorescence imaging and the osteogenic rate of the femur within osteoporosis treatment models, respectively. The group treated with reprogrammed MSCs exhibited a notably higher osteogenic rate, indicating augmented bone formation and repair capabilities.

Cell-sheet/HA-TCP "sandwich" constructs were transplanted locally into critical-sized calvarial defects in rats (Figure S2A and C) to evaluate their capacity for cranial bone regeneration. Figures 7I-M present microCT results and bone parameters for reprogrammed MSCs in the context of cranial defect repair. Consistent with the osteoporosis treatment, the group treated with reprogrammed MSCs exhibited substantial enhancements in bone regeneration (Fig. 7I), characterized by increased bone volume (Fig. 7J-L) and decreased trabecular spacing (Fig. 7M) when compared to the group treated with BRONJ MSCs. H&E staining of skulls revealed an increase in new bone formation in the Defect + reprogrammed MSCs group as opposed to the Defect + BRONJ MSCs group (Fig. 7 N). Consistent with the in vitro findings described above, the two animal models further demonstrated that reprogrammed MSCs maintain a strong osteogenic capacity in vivo, an effect attributed to the therapeutic action of miR-145-3p-enriched exosomes.

In sum, we pinpoint the miR-145-3p/IREB2/ferroptosis axis as the key regulator of BRONJ pathogenesis and show that miR-145-3p-loaded exosomes simultaneously resolve jaw necrosis and restore the systemic bone-forming capacity of endogenous MSCs, providing a potential therapy against BRONJ, as summarized in Fig. 8.

Discussion

In this study, we have uncovered the critical role of miR-145-3p in the pathogenesis of BRONJ and demonstrated the potential of engineered exosomes as a therapeutic strategy to inhibit ferroptosis and enhance osteonecrosis repair. Our findings firstly reveal that BRONJ is associated with increased ferroptosis in jawbone MSCs, as evidenced by elevated iron levels, MDA and ROS, along with reduced GPX4 expression and mitochondrial

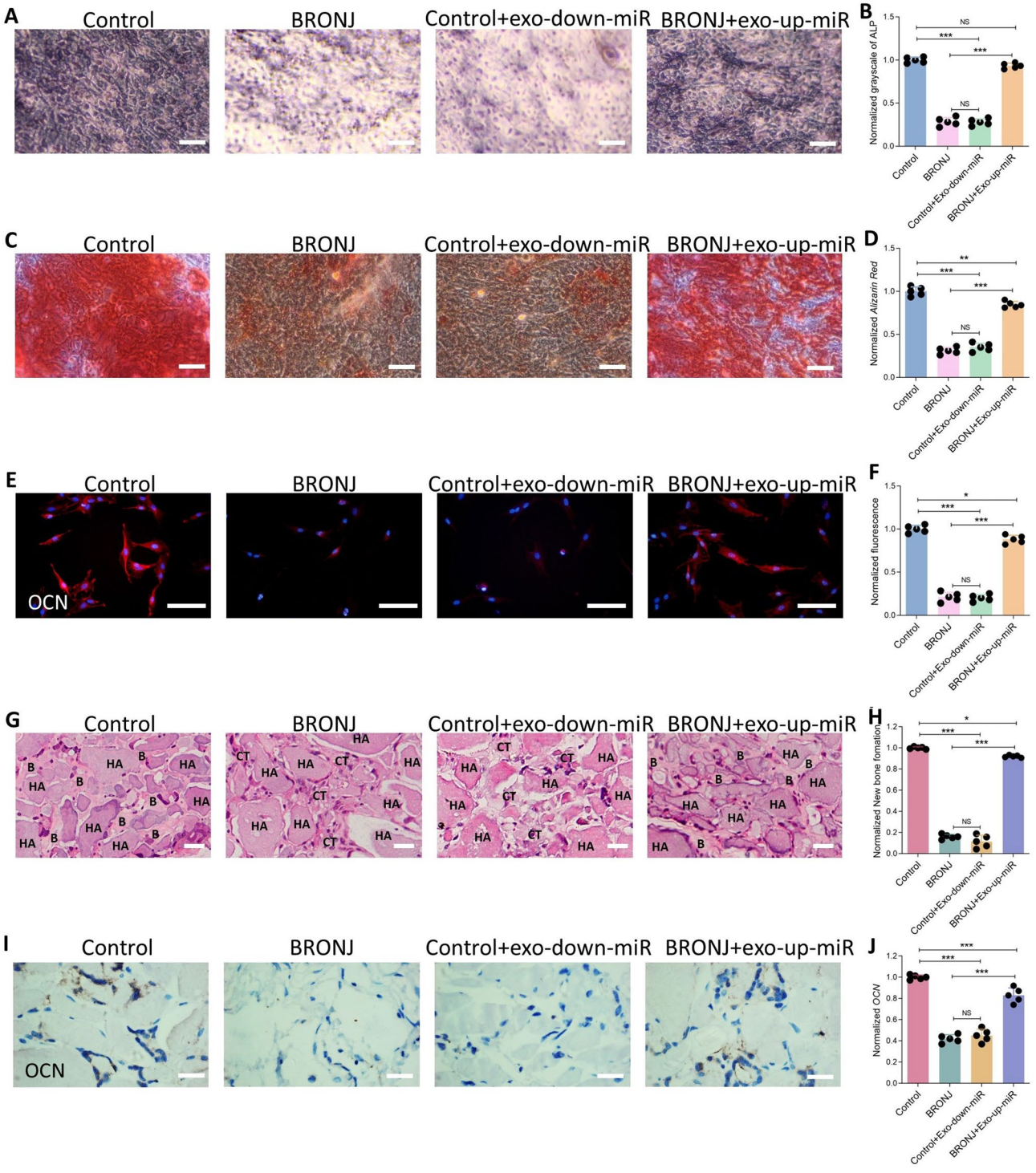

Fig. 6 Exosome-mediated Delivery of miR-145-3p Attenuates Ferroptotic Stress and Potentiates the Osteogenic Capacity of Resident MSCs within BRONJ Lesions. (**A**) ALP staining of MSCs and its (**B**) quantitative analysis. (**C**) Mineralized nodules formation of MSCs and its (**D**) quantitative analysis. Scale bar, 20 μm. (**E**) Immunofluorescence staining of OCN expression in MSCs and its (**F**) quantitative analysis. Scale bar, 10 μm. (**G**) H&E staining of subcutaneous ectopic ossification induced by MSCs transplantation in nude mice (HA: HA-TCP, B: new bone, CT: connective tissue) and its (**H**) quantitative analysis. Scale bar, 50 μm. (**I**) Immunohistochemical staining of OCN expression in MSCs of subcutaneous grafts (seven days after transplantation) and its (**F**) quantitative analysis. Scale bar, 20 μm. Data are presented as means ± SD ($n = 5$). *$p < 0.05$; **$p < 0.01$; ***$p < 0.001$

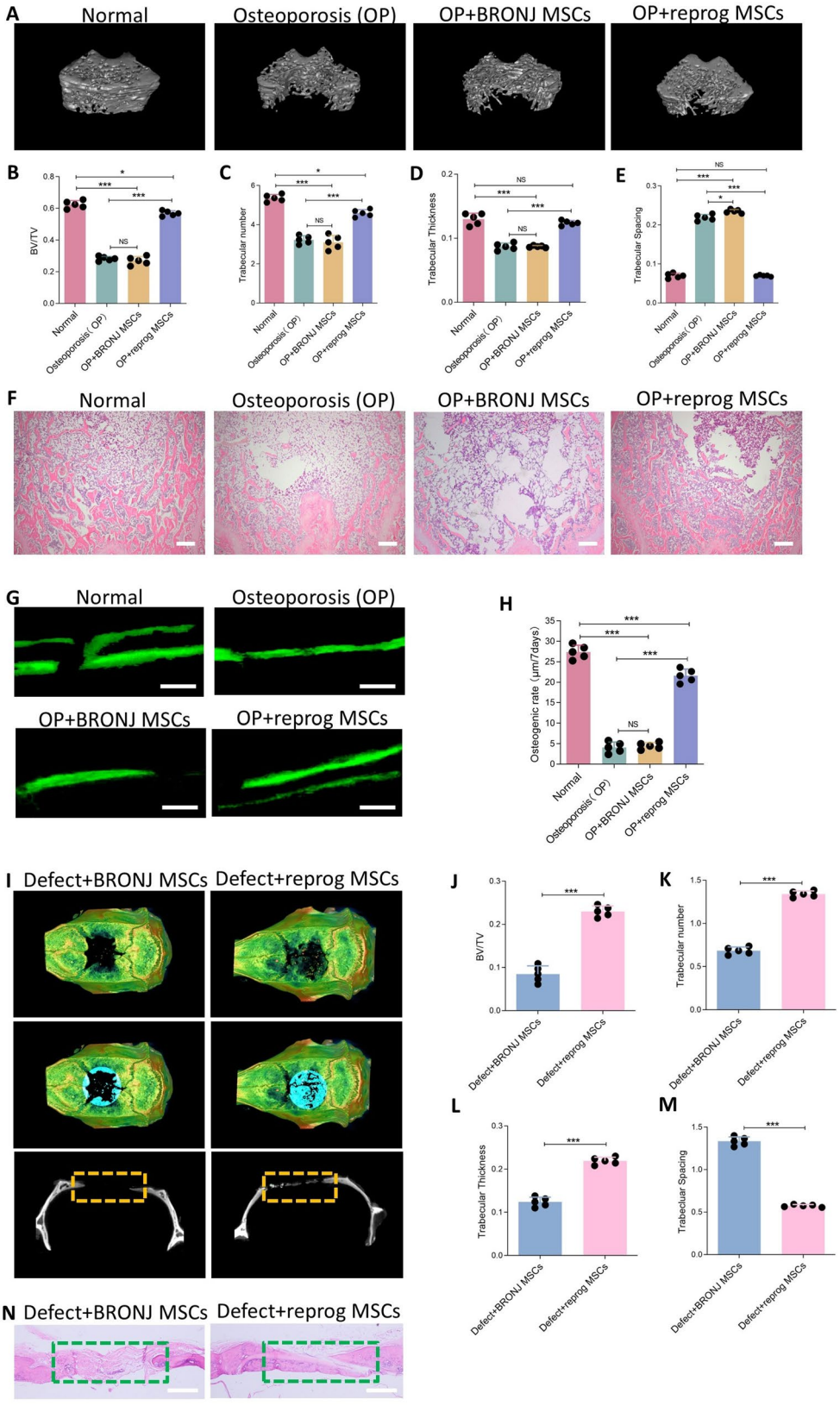

Fig. 7 (See legend on next page.)

(See figure on previous page.)

Fig. 7 Exosome-Reprogrammed BRONJ-Derived MSCs Restore Osteogenesis in Osteopenic and Unloaded Environments. (**A**) The 3D morphology, (**B**) BV/TV, (**C**)Trabecular number, (**D**)Trabecular thickness and (**E**)Trabecular space of the femurs in Control group, OP group, OP + BRONJ MSCs group and OP + reprog MSCs group. (**F**) H&E staining of femurs in Control group, OP group, OP + BRONJ MSCs group and OP + reprog MSCs group. Scale bar, 250 μm. (**G**) Calcein labeling and its (**H**) quantitative analysis of femurs in Control group, OP group, OP + BRONJ MSCs group and OP + reprog MSCs group. Scale bar, 50 μm. (**I**) The 3D morphology, (**J**) BV/TV, (**K**) Trabecular number, (**L**) Trabecular thickness and (**M**) Trabecular space of the calvarial defect in Defect + BRONJ MSCs group and Defect + reprog MSCs group. (**N**) H&E staining of calvarial defect in Defect + BRONJ MSCs group and Defect + reprog MSCs group. Scale bar, 150 μm. Note: OP + reprog MSCs: OP + reprogrammed MSCs. Data are presented as means ± SD ($n = 5$). *$p < 0.05$; **$p < 0.01$; ***$p < 0.001$

dysfunction. The overexpression of miR-145-3p and the subsequent inhibition of ferroptosis led to improved cell survival and osteogenic differentiation. Furthermore, localized transplantation of miR-145-3p-enriched exosomes robustly rescues the osteogenic differentiation capacity of endogenous MSCs and effectively ameliorates osteonecrosis in BRONJ, suggesting a novel mechanism by which miR-145-3p may regulate bone homeostasis in the context of BRONJ.

In this study, we intentionally selected reprogrammed MSCs, rather than direct exosome administration, for treating osteoporosis and calvarial defects, guided by three mechanistic and translational rationales: (i) Osteoporotic bone is populated by MSCs with markedly blunted osteogenic competence [27], and the cranial defect niche is similarly deprived of functionally primed progenitors [28]. One of key mechanisms underlying the therapeutic effects of systemically injected MSCs in osteoporosis is their targeted homing to bone tissue followed by direct participation in osteogenic differentiation [29]. Additionally, because the calvarium develops through intramembranous ossification, the transplanted MSCs repair calvarial defects by directly participating in osteogenic differentiation [30]. Therefore, we employed these two in vivo animal models to verify that osteogenic differentiation capacity is indeed restored in BRONJ-derived MSCs after exosome treatment. In fact, transplantation of reprogrammed MSCs into OVX-induced osteoporotic rats and critical-sized calvarial defects provides in vivo proof that epigenetic reprogramming restores robust osteogenic capacity, thereby validating our central hypothesis. (ii) Mounting evidence implicates iron-metabolic dysregulation in both osteoporosis [31, 32] and osseous repair failure [33, 34]. We demonstrate that reprogrammed MSCs harvested from miR-145-3p-conditioned BRONJ rats retain not only elevated intracellular miR-145-3p but also secrete exosomes enriched with this miRNA. Consequently, reprogrammed MSCs may act as self-sustaining vectors that re-engineer the local iron-metabolic microenvironment and normalize aberrant ferroptotic signaling in both pathological contexts. (iii) Utilizing autologous, disease-rescued MSCs circumvents the immunologic and logistical constraints inherent to allogeneic transplantation. By epigenetically rejuvenating patient-derived MSCs that were initially dysfunctional, this work outlines a preliminary framework that, with further validation, may be adapted to other MSC-related disorders.

Iron overload precipitates MSCs ferroptosis, a ROS-driven death pathway that arrests osteoblast lineage commitment while shifting differentiation toward adipogenesis, thereby tilting bone remodeling toward net resorption [34–36]. Our findings align with emerging evidence positioning iron dyshomeostasis as a central disruptor of skeletal homeostasis. We extend this paradigm by causally anchoring ferroptosis to BRONJ pathogenesis and pinpointing miR-145-3p as the pivotal epigenetic checkpoint governing the process. The role of miR-145 in modulating ferroptosis has been previously reported in some cell types [18, 19], but our work is among the first to explore its function in BRONJ-affected MSCs. Current evidence consolidates the molecular determinants by which iron metabolism governs MSCs osteogenic differentiation into four mechanistic tiers: (i) Iron homeostatic pathway: in this process, key constituents of the iron-metabolic machinery function as principal targets that orchestrate downstream regulation. For instance, CRYAB has been shown to bind and stabilize FTH1, thereby preventing iron release and ferroptosis, ultimately promoting osteogenic differentiation [37]. (ii) Antioxidant/ferroptosis defense systems signaling: in such pathways, collapse of the antioxidant stress response elevates intracellular ROS in MSCs, thereby precipitating ferroptosis. For example, the PI3K/AKT/mTOR signaling pathway has been implicated in protecting MSCs from ferroptosis by regulating iron uptake and ROS production [38]. (iii) Energy metabolism-related pathways: in this class of mechanisms, dysregulation of energy metabolism can act as either a cause or a consequence of ferroptosis. For instance, mitochondrial damage is closely associated with the induction of ferroptosis in various cell types, including MSCs [39, 40]. Conversely, elevated iron levels and oxidative stress disrupt the mitochondrial function, reducing the cells' ability to produce energy and synthesize osteogenic proteins such as RUNX2 and OCN [41]. This iron-mediated mitochondrial dysfunction not only inhibits osteogenesis but also shifts the differentiation fate of MSCs towards adipogenesis, further disrupting bone homeostasis [41]. (iv) Epitranscriptomic and signaling crosstalk: epigenetic modulation and signal crosstalk are defining hallmarks of this mechanistic class. For example, METTL16-mediated N6-methyladenosine (m^6A) modification of PPARγ

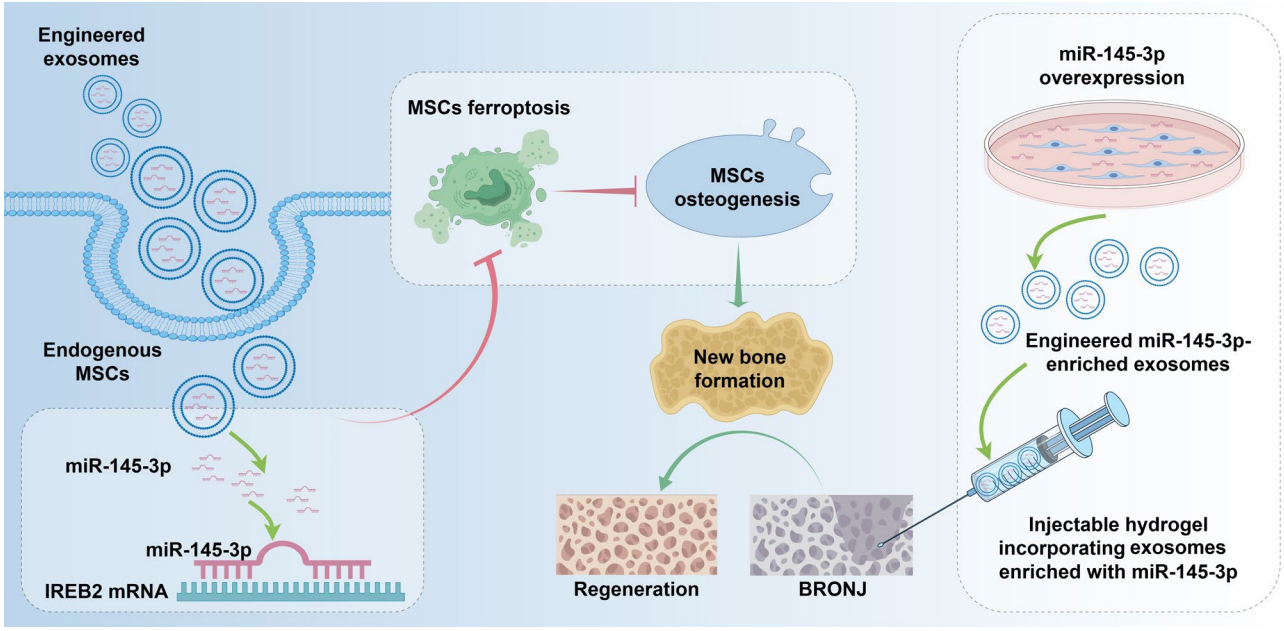

Fig. 8 Schematic diagram of the study. (Supported by Figdraw 2.0 biological illustration platform (https://www.figdraw.com/) (Copyright export ID: APSPW7d76d)

mRNA promotes lipid remodeling and ferroptosis, indirectly constraining MSCs osteogenesis [42]. Our identification of a miRNA-directed ferroptosis axis that governs MSC osteogenesis represents a distinct epigenetic regulator within this mechanistic spectrum. In future work, we will deepen our mechanistic exploration of ferroptosis-driven BRONJ progression. Our immediate priorities are to map the complete regulatory network surrounding the miR-145-3p/IREB2 axis and to define how ferroptosis operates in a cell-type-specific manner within the BRONJ lesion, thereby identifying more precise therapeutic targets. In parallel, we will profile additional signaling implicated in BRONJ pathogenesis and elucidate how they interact with ferroptotic pathways. Finally, we will dissect how exosome-mediated intercellular signaling remodels the pathological niche, aiming to uncover druggable targets within the BRONJ microenvironment.

Emerging evidence positions MSCs-based therapy as the most multifaceted regenerative platform for BRONJ. Conceptually, four mechanistic axes are currently explored: (i) Exogenous MSCs home to necrotic bone and re-activate endogenous osteoprogenitors, directly restoring bone defect through paracrine crosstalk [43]; (ii) Topically delivered MSCs orchestrate gingival-mucosal re-epithelialization and collagen remodeling, sealing exposed bone and preventing secondary infection [44, 45]; (iii) Secreted factors from MSCs up-regulate PDGF signaling, synchronizing osteogenic-angiogenic coupling and neo-angiogenesis within both osseous and mucosal compartments [46, 47]; (iv) MSCs exert potent immunomodulation, rebalancing Th17/Treg [48] or M1/M2 macrophages [49] phenotypes and inhibiting pathogenic inflammation, thereby creating an immune-permissive niche for tissue repair. From a translational standpoint, delivery modalities have diversified into five tiers: (i) direct cell therapy via systemic infusion or local implantation of bone-marrow-, adipose-, umbilical cord-derived MSCs [43]; (ii) cell-free intervention with MSCs-derived extracellular vesicles, which recapitulate the paracrine secretome while circumventing the risks of live-cell transfer [50]; (iii) purified MSCs-secreted cytokines or recombinant proteins (e.g., MCP-1, IGF-1, VEGF and PDGF-BB) administration [46, 51]; and (iv) bioengineered scaffolds that spatially immobilize MSCs within osteoinductive matrices (e.g., bioactive glasses) to achieve spatiotemporally controlled release [52]; and (v) exogenous pharmaceuticals that act directly on MSCs [53–55]. Our group has recently uncovered ferroptosis as a previously unrecognized driver of MSCs attrition and impaired osteogenic commitment within the BRONJ microenvironment. Capitalizing on this insight, we have engineered MSCs-derived exosomes that are enriched in miR-145-3p. These exosomes not only neutralize lipid-ROS accumulation in resident MSCs but also reactivate osteogenic signaling, thereby rescuing endogenous bone-forming capacity. This ferroptosis-targeted, exosome-based strategy may represent a paradigm shift in BRONJ therapeutics, integrating cell-free safety with mechanism-specific precision.

Compared to traditional surgical and pharmacological treatments for BRONJ [1, 2], our exosome-mediated miR-145-3p therapy offers several unique advantages.

Unlike surgical debridement, which is invasive and carries a risk of complications, our approach is minimally invasive and can be delivered systemically or locally. Additionally, compared to drug-based therapies that often have limited efficacy and potential side effects, our strategy targets a specific molecular pathway involved in BRONJ pathogenesis, thereby potentially reducing off-target effects [56]. Moreover, exosome-mediated delivery may bypass the compromised vasculature [56] typical of BRONJ lesions, ensuring that miR-145-3p reaches resident MSCs even in BRONJ-affected microenvironments where conventional topically applied drugs fail to penetrate. The endogenous origin of exosomes also minimizes immunogenicity and allows repeat dosing without eliciting neutralizing antibodies, a critical advantage over recombinant protein or viral therapies that lose efficacy after successive administrations [56]. However, it is worth noting that when BRONJ has progressed to extensive sequestrum and cortical plate collapse, exosome-based therapy alone cannot provide mechanical support; it must therefore be combined with debridement or bone grafting, or integrated with new scaffolds that possess superior biological properties.

Beyond BRONJ, ferroptosis has emerged as a unifying pathogenic node across a spectrum of osteonecrotic disorders, including radiation-induced osteonecrosis of the jaw (RONJ) [57], glucocorticoid-induced osteonecrosis of the femoral head (GONFH) [58, 59], and diabetes-associated osteonecrosis [60, 61]. These entities share core pathological motifs, namely, deranged osteoblastic-osteoclastic coupling, aberrant angiogenesis, and immune-metabolic microenvironment redirected toward oxidative stress and chronic inflammation, driven by ferroptotic damage in MSCs, endothelial cells and immune cells. Our previous study has demonstrated that, in RONJ, ionizing radiation redistributes lysosomes toward the perinuclear region, disrupting endothelial metabolism and catalyzing lipid peroxidation-driven ferroptosis [57]. Transplantation of exosomes derived from MSCs cell aggregates enables the delivery of lysosomes to achieve lysosomal redistribution, rescues endothelial integrity, improves $CD31^{+}$ $endomucin^{+}$ specialized vessels and mitigates jawbone necrosis [57]. Moreover, In GONFH, miRNAs have been implicated in modulating ferroptosis of MSCs, thereby rescuing their osteogenic differentiation capacity: a mechanistic parallel that our investigation mirrors [58, 59]. Diabetes mellitus, a well-established risk factor for osteonecrosis [62], amplifies systemic iron overload and lipotoxic ROS generation; emerging data implicate ferroptosis in diabetic bone microangiopathy, suggesting a mechanistic continuum with diabetes-related osteonecrotic phenotypes [63]. By synthesizing these mechanistic intersections, lysosomal trafficking in RONJ, miR-mediated redox circuitry in GONFH, and iron-lipid homeostasis in diabetic bone disease, we hope to delineate common therapeutic targets. Our primary goal is to explore this convergence to identify candidate targets common to multiple forms of osteonecrosis and to develop MSC- or exosome-based interventions that may ultimately be applicable beyond single etiologies.

Despite the novelty of our findings, particularly the first demonstration of ferroptosis in BRONJ and the therapeutic exploitation of exosomes targeting this pathway, the study has some limitations. Firstly, the evidence is restricted to in vitro assays and rodent models, mandating rigorous validation in human cohorts before any translational claim can be made. Secondly, although the miR-145-3p/IREB2 regulatory axis has been identified as a nexus between ferroptosis and osteogenesis, the wider signaling network governing these processes remains incompletely mapped. Third, we will pursue deeper mechanistic studies to develop advanced engineering strategies that both create precision-modified exosomes and design new biomaterial scaffolds, endowing exosome therapy with markedly improved targeting specificity and therapeutic efficacy. Finally, several pre-clinical obstacles must be overcome. Scalable, GMP-compliant production of exosomes with uniform physicochemical attributes and reproducible potency is currently lacking, and comprehensive toxicology, including biodistribution, immunogenicity, and long-term safety, has yet to be established. Future work should therefore prioritize (i) process optimization for high-yield, quality-controlled exosome manufacturing, and (ii) phased clinical trials to rigorously assess the efficacy and safety of miR-145-3p–loaded exosomes in BRONJ patients.

Conclusion

Collectively, our study identifies the miR-145-3p/IREB2/ferroptosis axis as the important regulator of BRONJ and demonstrates that exosomal delivery of miR-145-3p concurrently ameliorate localized jaw necrosis and markedly restores the systemic osteogenic potential of endogenous jawbone-derived MSCs. In this pre-clinical models, exosomal delivery of miR-145-3p attenuated local osteonecrosis and partially restored the osteogenic capacity of endogenous MSCs. While these results encourage further evaluation, additional studies are required to determine efficacy, safety, and generalizability to other bone-loss conditions before clinical translation.

Supplementary Information

The online version contains supplementary material available at https://doi.org/10.1186/s12951-025-03745-9.

Supplementary Material 1.

Acknowledgements
We sincerely thank Xiaolei Shi, Ke Liu, and Chenyu Zeng (Jinling Hospital, Affiliated Hospital of Medical School, Nanjing University) for their technical assistance in establishing the animal models, and we are equally grateful to Xinyao He (Jinling Hospital, Affiliated Hospital of Medical School, Nanjing University) for the invaluable technical support provided during the isolation and characterization of exosomes. We also express our heartfelt gratitude to the Figdraw 2.0 biological illustration platform (https://www.figdraw.com/) (Copyright export ID: APSPW7d76d, PUTTOc4c14) for their support with the bio-renderings in this study.

Author contributions
Yi Shuai: Conceptualization, Data curation, Formal analysis, Funding acquisition, Investigation, Methodology and Writing-original draft. Bo Chen and Tao Jiang: Conceptualization, Data curation, Funding acquisition and Investigation. Lei Zhu, Han Su and Wei Wei: Investigation and Methodology. Bingyao Liu and Lei Jin: Conceptualization, Funding acquisition, Project administration, Writing-review & editing.

Data availability
No datasets were generated or analysed during the current study.

Declarations

Ethics approval and consent to participate
All animal experimental protocols were reviewed and approved by the Department of Comparative Medicine at Jinling Hospital, Affiliated Hospital of Medical School, Nanjing University (Permit No. 2021DZGKJDWLS-0090), strictly adhering to the guidelines set forth by the NIH for the Care and Use of Laboratory Animals.

Consent for publication
Not applicable.

Competing interests
The authors declare no competing interests.

Author details
[1]Department of Stomatology, Jinling Hospital, Affiliated Hospital of Medical School, Nanjing University, Nanjing 210002, Jiangsu, China
[2]Department of Stomatology, General Hospital of Eastern Theater Command, PLA, Nanjing 210002, Jiangsu, China
[3]Department of Stomatology, Taikang Xianlin Drum Tower Hospital, Affiliated Hospital of Medical School, Nanjing University, Nanjing 210046, Jiangsu, China
[4]Department of Orthodontics & Prosthodontics, The Second Affiliated Hospital, Zhejiang University School of Medicine, Hangzhou 310009, Zhejiang, China

Received: 15 March 2025 / Accepted: 24 September 2025
Published online: 10 October 2025

References

1. Ruggiero SL, et al. American association of oral and maxillofacial surgeons' position paper on medication-related osteonecrosis of the jaws-2022 update. J Oral Maxillofac Surg. 2022;80(5):920–43.
2. Ruan HJ, et al. Chinese expert consensus on the diagnosis and clinical management of medication-related osteonecrosis of the jaw. J Bone Oncol. 2024;49:100650.
3. Jiang A, et al. Medication-related osteonecrosis of the jaw (MRONJ): a review of pathogenesis hypothesis and therapy strategies. Arch Toxicol. 2024;98(3):689–708.
4. Zheng J, Conrad M. Ferroptosis: when metabolism meets cell death. Physiol Rev. 2025;105(2):651–706.
5. Chen L, et al. Homeostasis and metabolism of iron and other metal ions in neurodegenerative diseases. Signal Transduct Target Ther. 2025;10(1):31.
6. Deng S, et al. *Lachnospiraceae*-bacterium alleviates ischemia-reperfusion injury in steatotic donor liver by inhibiting ferroptosis via the Foxo3-Alox15 signaling pathway. Gut Microbes. 2025;17(1):2460543.
7. Wang Y, et al. Targeted inhibition of ferroptosis in bone marrow mesenchymal stem cells by engineered exosomes alleviates bone loss in smoking-related osteoporosis. Mater Today Bio. 2025;31:101501.
8. Fan Y, et al. Isovitexin targets SIRT3 to prevent steroid-induced osteonecrosis of the femoral head by modulating mitophagy-mediated ferroptosis. Bone Res. 2025;13(1):18.
9. Wang D, et al. Mechanisms of ferroptosis in bone disease: a new target for osteoporosis treatment. Cell Signal. 2025;127:111598.
10. Dong Y, et al. A clinical-stage Nrf2 activator suppresses osteoclast differentiation via the iron-ornithine axis. Cell Metab. 2024;36(8):1679–95. .e6.
11. Xia Y, et al. Repin1 regulates iron metabolism and osteoblast apoptosis in osteoporosis. Cell Death Dis. 2023;14(9):631.
12. Luo C, et al. Canonical wnt signaling works downstream of iron overload to prevent ferroptosis from damaging osteoblast differentiation. Free Radic Biol Med. 2022;188:337–50.
13. Jiang Y, et al. Reducing PDK4 level constitutes a pivotal mechanism for glucocorticoids to impede osteoblastic differentiation through the enhancement of ferroptosis in mesenchymal stem cells. Stem Cell Res Ther. 2025;16(1):91.
14. Yalaev BI, et al. The role of MicroRNA in the regulation of differentiation and the functionality of osteoblasts, osteoclasts, and their precursors in osteoporosis. Noncoding RNA. 2025;11(1):14.
15. Zhou Q, et al. Amino acid metabolism disorder and oxidative stress took part in EGCG alleviating Mn-caused ferroptosis via miR-9-5p/got1 axis. J Hazard Mater. 2025;489:137656.
16. Yuan W, et al. Strontium-Alix interaction enhances exosomal miRNA selectively loading in synovial MSCs for temporomandibular joint osteoarthritis treatment. Int J Oral Sci. 2025;17(1):6.
17. Saverio V, et al. AKrs confer oligodendrocytes resistance to differentiation-stimulated ferroptosis. Redox Biol. 2025;79:103463.
18. Liang Z, et al. Silencing of lncRNA MALAT1 facilitates erastin-induced ferroptosis in endometriosis through miR-145-5p/MUC1 signaling. Cell Death Discov. 2022;8(1):190.
19. Zhou L, et al. Multi-omics analysis to identify CBR3-AS1-hsa-miR-145-5p-MAP3K5 pathway as a ferroptosis-related CeRNA network in benign prostatic hyperplasia. Genes Dis. 2024;11(5):101184.
20. Yang R, et al. Circulating microrna panel as a novel biomarker to diagnose bisphosphonate-related osteonecrosis of the jaw. Int J Med Sci. 2018;15(14):1694–701.
21. Gowtham A, Kaundal RK. Exploring the NcRNA landscape in exosomes: insights into wound healing mechanisms and therapeutic applications. Int J Biol Macromol. 2025;292:139206.
22. Liu L, et al. Hydrogels empowered mesenchymal stem cells and the derived exosomes for regenerative medicine in age-related musculoskeletal diseases. Pharmacol Res. 2025;213:107618.
23. Xue P et al. *Material-Mediated Immunotherapy to Regulate Bone Aging and Promote Bone Repair.* Small, 2025: p. e2409886.
24. Pan S, et al. Multifunctional injectable hydrogel microparticles loaded with miR-29a abundant BMSCs derived exosomes enhanced bone regeneration by regulating osteogenesis and angiogenesis. Small. 2024;20(16):e2306721.
25. Hu Y, et al. Oyster mantle-derived exosomes alleviate osteoporosis by regulating bone homeostasis. Biomaterials. 2024;311:122648.
26. Wu T, et al. Regulatory t cell-derived exosome mediated macrophages polarization for osteogenic differentiation in fracture repair. J Control Release. 2024;369:266–82.
27. Huo S, et al. Epigenetic regulations of cellular senescence in osteoporosis. Ageing Res Rev. 2024;99:102235.
28. Torres-Guzman RA, et al. Bone morphogenic protein and mesenchymal stem cells to regenerate bone in calvarial defects: a systematic review. J Clin Med. 2023;12(12):4064.
29. He XY, et al. Advances in the application of mesenchymal stem cells, exosomes, biomimetic materials, and 3D printing in osteoporosis treatment. Cell Mol Biol Lett. 2021;26(1):47.
30. Gou Y, et al. Adipose-derived mesenchymal stem cells (MSCs) are a superior cell source for bone tissue engineering. Bioact Mater. 2024;34:51–63.
31. Jiang Z, et al. Ferroptosis in osteocytes as a target for protection against postmenopausal osteoporosis. Adv Sci. 2024;11(12):e2307388.
32. Ye C, et al. Injectable natural Tremella-derived hydrogel for reversing ferroptosis-mediated osteoporotic microenvironment imbalance and promoting osteoregeneration. Biomaterials. 2025;324:123532.
33. Wang Z, et al. Oxygen-independent sulfate radical and Fe(2+)-modified implants for fast sterilization and osseointegration of infectious bone defects. ACS Nano. 2025;19(19):18804–23.

34. Jing Z, et al. Simvastatin/hydrogel-loaded 3D-printed titanium alloy scaffolds suppress osteosarcoma via TF/NOX2-associated ferroptosis while repairing bone defects. Bioact Mater. 2024;33:223–41.
35. Yang Y, et al. A two-pronged approach to inhibit ferroptosis of MSCs caused by the iron overload in postmenopausal osteoporosis and promote osseointegration of titanium implant. Bioact Mater. 2024;41:336–54.
36. Ruan B, et al. DNMT aberration-incurred GPX4 suppression prompts osteoblast ferroptosis and osteoporosis. Bone Res. 2024;12(1):68.
37. Tian B, et al. CRYAB suppresses ferroptosis and promotes osteogenic differentiation of human bone marrow stem cells via binding and stabilizing FTH1. Aging. 2024;16(10):8965–79.
38. Lan D, et al. Tocopherol attenuates the oxidative stress of BMSCs by inhibiting ferroptosis through the PI3k/AKT/mTOR pathway. Front Bioeng Biotechnol. 2022;10:938520.
39. Yang Y, et al. MGST1 overexpression ameliorates mitochondrial dysfunction and ferroptosis during myocardial ischemia/reperfusion injury after heart transplantation. Int J Biol Macromol. 2025;299:140135.
40. Xiong Z, et al. Human umbilical cord-derived mesenchymal stem cells attenuate liver fibrosis by inhibiting hepatocyte ferroptosis through mitochondrial transfer. Free Radic Biol Med. 2025;231:163–77.
41. He Y, et al. Molecular mechanism of mitochondrial autophagy mediating impaired energy metabolism leading to osteoporosis. Biochimica et Biophysica Acta (BBA). 2025;1871(3):167685.
42. Lu L, et al. Role of METTL16 in PPARγ methylation and osteogenic differentiation. Cell Death Dis. 2025;16(1):271.
43. Mazreku M, et al. Recent stem-cell-based and stem-cell-free possibilities for the therapeutic management of the osteonecrosis of the jaw. Biomolecules. 2025;15(4):595.
44. Zang X, et al. Adipose-derived stem cells prevent the onset of bisphosphonate-related osteonecrosis of the jaw through transforming growth factor β-1-mediated gingival wound healing. Stem Cell Res Ther. 2019;10(1):169.
45. Li M, et al. Characterization of mesenchymal stem cells derived from Bisphosphonate-Related osteonecrosis of the jaw patients' gingiva. Stem Cell Rev Rep. 2022;18(1):378–94.
46. Gao SY, et al. PDGF-BB exhibited therapeutic effects on rat model of bisphosphonate-related osteonecrosis of the jaw by enhancing angiogenesis and osteogenesis. Bone. 2021;144:115117.
47. Huang J, Wang L, Tian W. Small extracellular vesicles derived from adipose tissue prevent bisphosphonate-related osteonecrosis of the jaw by promoting angiogenesis. Int J Nanomed. 2021;16:3161–72.
48. Kikuiri T, et al. Cell-based immunotherapy with mesenchymal stem cells cures bisphosphonate-related osteonecrosis of the jaw-like disease in mice. J Bone Miner Res. 2010;25(7):1668–79.
49. Zheng Y, et al. Exosomes from Adipose-Derived mesenchymal stromal cells prevent Medication-Related osteonecrosis of the jaw by inhibiting macrophage M1 polarization and pyroptosis. Int J Nanomed. 2024;19:12675–93.
50. Watanabe J, et al. Extracellular vesicles of stem cells to prevent BRONJ. J Dent Res. 2020;99(5):552–60.
51. Ogata K, et al. Cytokine mixtures mimicking secretomes from mesenchymal stem cells improve medication-related osteonecrosis of the jaw in a rat model. JBMR Plus. 2018;2(2):69–80.
52. Kaibuchi N, et al. Cell therapy for medication-related osteonecrosis of the jaw: update on treatment strategies. Eur Cells Mater. 2021;41:31–9.
53. Song J, et al. LINC01013 reverses bisphosphonate-impaired osteogenic differentiation of JBMMSCs by regulating intracellular translocation of ILF3. Stem Cell Res Ther. 2025;16(1):319.
54. Jin Y, et al. Betaine alleviates bisphosphonate-related osteonecrosis of the jaw by rescuing BMSCs function in an m6A-METTL3-dependent manner. Int J Mol Sci. 2025;26(11):5233.
55. Du Q, et al. Beta-adrenergic receptor antagonist propranolol prevents bisphosphonate-related osteonecrosis of the jaw by promoting osteogenesis. J Dent Sci. 2025;20(1):539–52.
56. Deng L, et al. Exosomes to exosome-functionalized scaffolds: a novel approach to stimulate bone regeneration. Stem Cell Res Ther. 2024;15(1):407.
57. Li YY, et al. Lysosome-featured cell aggregate-released extracellular vesicles regulate iron homeostasis and alleviate post-irradiation endothelial ferroptosis for mandibular regeneration. Adv Sci. 2025;12(34):e05070.
58. Zuo R, et al. MiR-370-3p regulate TLR4/SLC7A11/GPX4 to alleviate the progression of glucocorticoids-induced osteonecrosis of the femoral head by promoting osteogenesis and suppressing ferroptosis. J Orthop Translat. 2025;51:337–58.
59. Zheng L, et al. Knockdown of Gfi1 increases BMSCs exosomal miR-150-3p to inhibit osteoblast ferroptosis in steroid-induced osteonecrosis of the femoral head through BTRC/Nrf2 axis. Endocr J. 2025;72(2):205–19.
60. Jin C, et al. A novel anti-osteoporosis mechanism of VK2: interfering with ferroptosis via AMPK/SIRT1 pathway in type 2 diabetic osteoporosis. J Agric Food Chem. 2023;71(6):2745–61.
61. Xu CY, et al. Poliumoside protects against type 2 diabetes-related osteoporosis by suppressing ferroptosis via activation of the Nrf2/GPX4 pathway. Phytomedicine. 2024;125:155342.
62. Cheng EY, et al. How are Diabetes, Statins, and immunosuppressive medications linked to Non-Traumatic osteonecrosis of the femoral head in kidney transplant recipients? J Arthroplasty. 2025;2(25):S0883–5403.
63. Yu H, et al. Targeting ferroptosis with natural products to treat diabetes and its complications: opportunities and challenges. Phytother Res; 2025.

Publisher's note